Joule

CellPress
OPEN ACCESS

Article

Operando visualization of kinetically induced lithium heterogeneities in single-particle layered Ni-rich cathodes

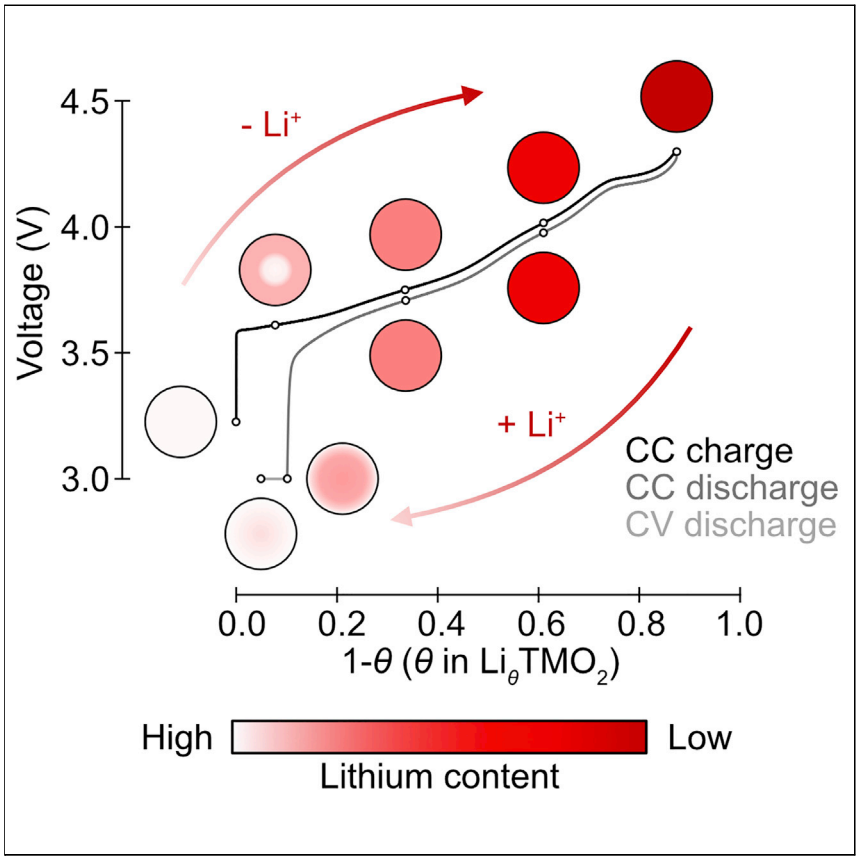

Optical scattering microscopy reveals lithium heterogeneity in NMC cathodes.

Chao Xu, Alice J. Merryweather, Shrinidhi S. Pandurangi, ..., Christoph Schnedermann, Akshay Rao, Clare P. Grey

cs2002@cam.ac.uk (C.S.)
ar525@cam.ac.uk (A.R.)
cpg27@cam.ac.uk (C.P.G.)

Highlights

Optical scattering microscopy reveals lithium heterogeneity in NMC single crystals

Charging and discharging in NMC kinetically limited by concentration-dependant diffusivity

Results explain ~10% capacity loss in NMC during the first cycle

Xu et al., Joule 6, 1–12
November 16, 2022
Published by Elsevier Inc.
https://doi.org/10.1016/j.joule.2022.09.008

Please cite this article in press as: Xu et al., Operando visualization of kinetically induced lithium heterogeneities in single-particle layered Ni-rich cathodes, Joule (2022), https://doi.org/10.1016/j.joule.2022.09.008

Joule

CellPress
OPEN ACCESS

Article

Operando visualization of kinetically induced lithium heterogeneities in single-particle layered Ni-rich cathodes

Chao Xu,[1,2,3,4,6] Alice J. Merryweather,[1,2,3,6] Shrinidhi S. Pandurangi,[3,5,6] Zhengyan Lun,[1,2,3] David S. Hall,[1,3] Vikram S. Deshpande,[3,5] Norman A. Fleck,[3,5] Christoph Schnedermann,[2,3,*] Akshay Rao,[2,3,*] and Clare P. Grey[1,3,7,*]

SUMMARY

Understanding how lithium-ion dynamics affect the (de)lithiation mechanisms of state-of-the-art nickel-rich layered oxide cathodes is crucial to improve electrochemical performance. Here, we directly observe two distinct kinetically induced lithium heterogeneities within single-crystal $LiNi_xMn_yCo_{(1-x-y)}O_2$ (NMC) particles using recently developed *operando* optical microscopy, challenging the notion that uniform (de)lithiation occurs within individual particles. Upon delithiation, a rapid increase in lithium diffusivity at the beginning of charge results in particles with lithium-poor peripheries and lithium-rich cores. The slow ion diffusion at near-full lithiation states—and slow charge transfer kinetics—also leads to heterogeneity at the end of discharge, with a lithium-rich surface preventing complete lithiation. Finite-element modeling confirms that concentration-dependent diffusivity is necessary to reproduce these phenomena. Our results demonstrate how kinetic limitations cause significant first-cycle capacity losses in Ni-rich cathodes.

INTRODUCTION

Layered Ni-rich NMCs ($LiNi_xMn_yCo_{(1-x-y)}O_2$, $x \geq 0.5$) and NCAs ($LiNi_xCo_yAl_{(1-x-y)}O_2$, $x \geq 0.5$) are widely used as cathode materials in high-energy-density lithium-ion batteries for electric vehicle applications.[1–4] Despite their cost and environmental benefits, these cathode materials suffer from long-term stability issues that limit their safety and lifetime, as well as typical irreversible capacity losses of >10% during the first cycle.[5–7] Significant world-wide effort is thus being devoted to understanding their underlying charging mechanisms to mitigate these shortcomings.[3,8,9] Previous studies have attributed the first-cycle capacity losses to kinetic limitations due to slow lithium diffusion at near-full lithiation states as a result of fewer lithium vacancies and decreased interlayer spacing.[10,11] X-ray diffraction (XRD)-based methods have furthermore revealed several "phase segregation" phenomena during the delithiation of Ni-based layered cathodes,[12–15] despite the fact that the (de)lithiation of such materials intrinsically follows a solid-solution mechanism.[12,16,17] Rather than a thermodynamic phase segregation, these observations suggest formation of kinetically controlled heterogeneities in lithium occupancy that occur over a sufficient domain size or length scale to result in discernible differences in the lattice constants and diffraction signals; however, a debate exists as to whether this heterogeneity is at the particle or electrode level.[14]

CONTEXT & SCALE

The mechanism by which lithium ions are stored in high-energy-density lithium-ion battery materials is typically assumed to be uniform across the individual active particles. Here, by using *operando* optical scattering microscopy and diffusive modeling, the authors directly image and track the buildup of kinetically induced lithium-ion heterogeneity within individual particles during battery operation in one of the most promising next-generation cathode materials based on nickel-rich manganese cobalt oxide (NMC).

The insights provided by this study do not only challenge long-held beliefs but also motivate new approaches to overcome critical capacity losses in high-performance materials, especially as society moves toward fast-charging regimes.

These proposed lithium heterogeneity phenomena are closely correlated with the electrochemical performance of the cathode material. However, our understanding of the operative mechanism by which the heterogeneity arises at the particle level is limited since many of these studies are based on ensemble characterization techniques, particularly *in situ* and *ex situ* XRD of bulk electrodes, where the measurements inherently cannot spatially resolve the heterogeneity at the relevant length scales.[12,13] Recent advances in synchrotron-based micro-spectroscopy techniques, such as scanning transmission X-ray microscopy (STXM) coupled with X-ray absorption spectroscopy,[14,18–20] are capable of providing chemical information at the nanometer scale. However, such techniques suffer from disadvantages including limited availability of beam time and potential beam damage.[21]

In this work, we directly track the lithium-ion dynamics in monolithic (also referred to as "single-crystal") Ni-rich NMC cathodes, with a particular focus on the transient lithium heterogeneities during lithium insertion and extraction, using a recently developed method—*operando* optical scattering microscopy.[22] Our results demonstrate a clear correlation between the optical intensity and local lithium content, and we identify kinetically induced lithium heterogeneities within individual active NMC particles. These heterogeneities are most prominent at the beginning of the charge and also appear at the end of discharge, originating from a sharp drop in the lithium-ion diffusion coefficient toward high lithium contents. We further explore the origins of these phenomena with finite-element modeling parameterized by a lithium concentration-dependent diffusion coefficient, derived from solid-state nuclear magnetic resonance (ssNMR) characterization. This combined approach enables us to determine the effects of the rate-limiting kinetic processes on the (de)lithiation of Ni-rich NMC cathodes and identify the conditions under which lithium heterogeneity occurs at the individual particle level. Via experiment and theory, we determine the origin of the first-cycle capacity loss in NMCs.

RESULTS

Operando optical scattering microscopy

During a typical *operando* measurement, an optically accessible electrochemical cell (Figure 1A) operates either under a constant-current (CC) or a constant-voltage (CV) bias and is simultaneously illuminated with a light-emitting diode (LED, central wavelength of 740 nm). The reflected and back-scattered light from the sample and the glass/electrolyte interface is collected and imaged onto a camera. Figure 1B shows an optical image of part of the NMC cathode with nominal stoichiometry $LiNi_{0.87}Mn_{0.05}Co_{0.08}O_2$, where the bright area corresponds to an individual ~2 μm NMC particle and the surrounding dark area represents the conductive carbon and binder matrix. The observed optical intensity is primarily determined by the local dielectric properties of the particle,[23–25] which are sensitive to the degree of lithiation.

The uniform optical intensity across the particle suggests that the top surface is smooth and flat, as further confirmed by a scanning electron microscope (SEM) image of the same particle (Figure 1C). Moreover, the flat surface is a strong indication that the observed surface is parallel to the NMC a/b basal plane (see the structure illustration in Figure 1D), which is further supported by the *operando* optical results discussed below.

XRD confirms the NMC is phase pure (space group $R\bar{3}m$) and has a low Li/Ni antisite mixing (~2%; diffraction pattern and Rietveld refinement results are shown in

[1]Yusuf Hamied Department of Chemistry, University of Cambridge, Cambridge, UK

[2]Cavendish Laboratory, University of Cambridge, Cambridge, UK

[3]The Faraday Institution, Quad One, Harwell Science and Innovation Campus, Didcot, UK

[4]School of Physical Science and Technology, ShanghaiTech University, Shanghai, China

[5]Department of Engineering, University of Cambridge, Cambridge, UK

[6]These authors contributed equally

[7]Lead contact

*Correspondence: cs2002@cam.ac.uk (C.S.), ar525@cam.ac.uk (A.R.), cpg27@cam.ac.uk (C.P.G.)

https://doi.org/10.1016/j.joule.2022.09.008

Please cite this article in press as: Xu et al., Operando visualization of kinetically induced lithium heterogeneities in single-particle layered Ni-rich cathodes, Joule (2022), https://doi.org/10.1016/j.joule.2022.09.008

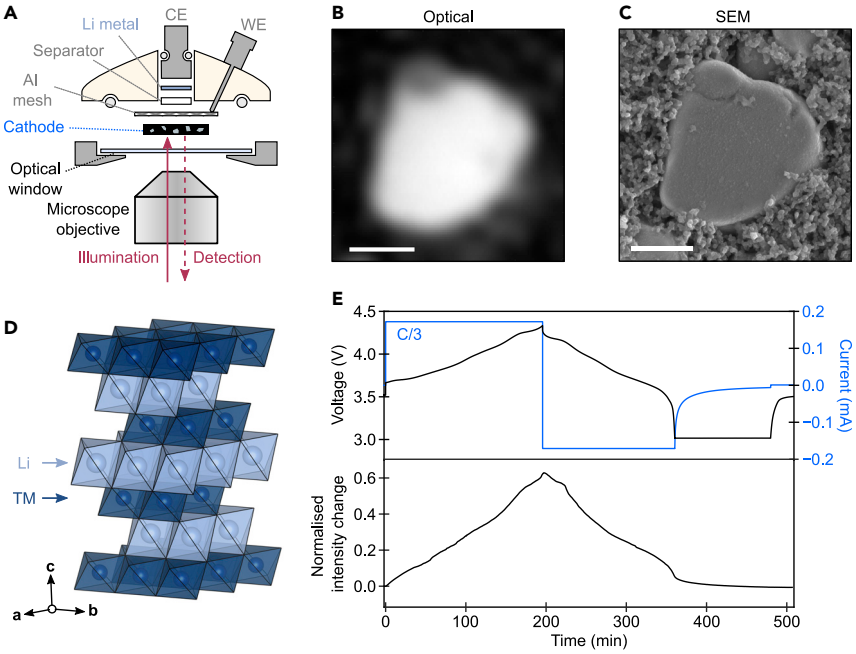

Figure 1. Monolithic NMC cathode and *operando* optical microscopy

(A) Schematic drawing of the key components of the electrochemical cell for optical microscopy. The cathode is a self-standing electrode composed of numerous NMC particles, carbon black and polytetrafluoroethylene (PTFE) binder. Aluminum mesh is used as a current collector (WE, working electrode; CE, counter electrode).

(B) Optical image of an active NMC particle in the electrochemical cell.

(C) SEM image of the same monolithic NMC particle shown in (B), obtained after the optical measurements.

(D) Schematic illustration of the crystal structure of the NMC cathode illustrating the alternating layers of LiO_6 and TMO_6 octahedra, where TM denotes transition metal.

(E) Voltage (black) and current (blue) profile (top panel) and the normalized optical intensity of the active particle shown in (B) (bottom panel) during one charge-discharge cycle (comprising a C/3 constant-current [CC] charge and discharge between 4.3 and 3 V, followed by a 2-h constant-voltage [CV] hold at 3 V). Three C/3 cycles were performed prior to this cycle, finishing with 2-h voltage holds at 3 V. The C-rate was calculated based on a practical capacity of 210 mA h g^{-1}, i.e., the current density for the C/3 rate is 70 mA g^{-1}. Scale bars, 1 μm.

Figure S5). Figure 1E shows a typical voltage (black line) and current (blue line) profile for a CC charge—CCCV discharge cycle at a C/3 rate (*n*C corresponds to a full charge or discharge in 1/*n* hours), with a 2-h voltage hold at 3 V at the end of discharge (full electrochemical cycling history is summarized in Figure S6). The CC charge and CC discharge capacities were 229.0 and 192.4 mA h g^{-1}, respectively, corresponding to a coulombic efficiency (CE) of 84.0%. The 2-h hold at 3 V provided an additional 16.4 mA h g^{-1}, increasing the CE to 91.2%. The extra discharge capacity obtained by applying a CV step at the end of CC discharge is a generic behavior for all layered Ni-rich cathodes.[5,13] Note that even with a CV hold, the CE of 91.2% is lower than that achieved in coin cells with an equivalent electrode and cycling procedure (typically >99% after the first cycle; see Figure S7), which we attribute to the performance limitations of the specialized *operando* cell.

On charge, the optical intensity of the active particle increases monotonically as lithium is de-intercalated from the NMC particle, reaching a maximum intensity ~62% higher than its initial value; the general trend is reversed on discharge/lithiation (bottom panel in Figure 1E; Video S1). This clearly shows that the dielectric

Please cite this article in press as: Xu et al., Operando visualization of kinetically induced lithium heterogeneities in single-particle layered Ni-rich cathodes, Joule (2022), https://doi.org/10.1016/j.joule.2022.09.008

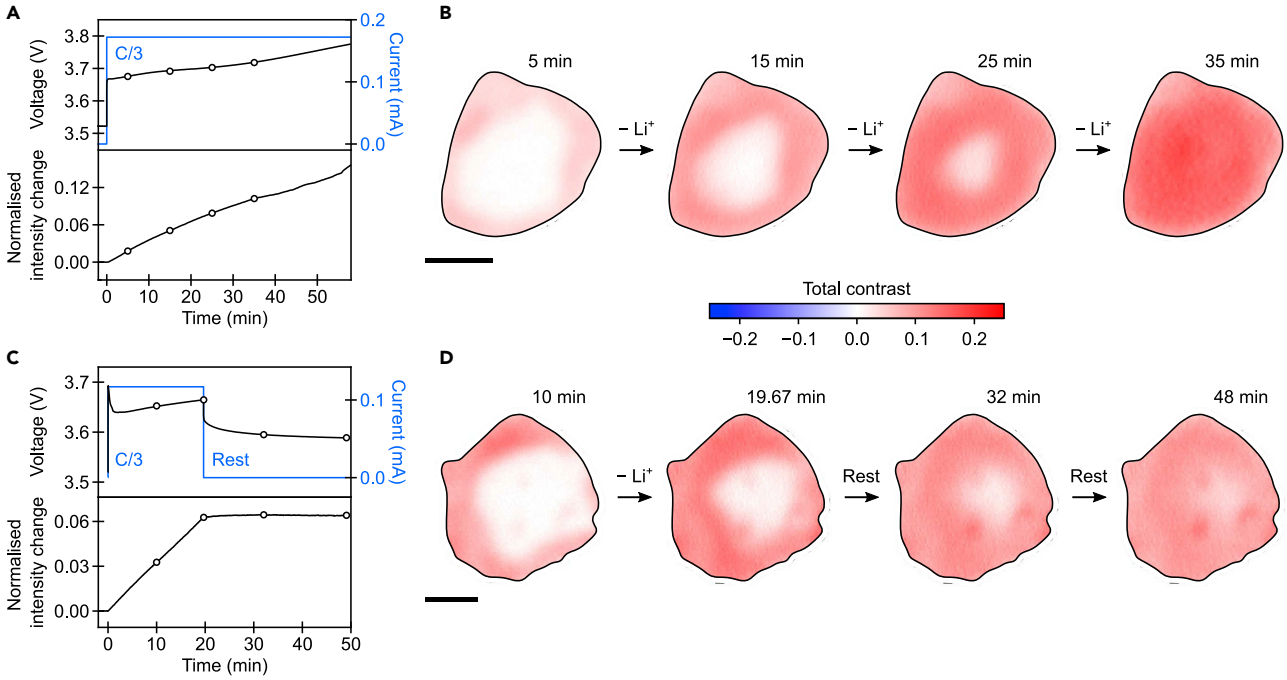

Figure 2. Lithium heterogeneity in single-particle NMC at the beginning of charge

(A) Voltage and current profiles during the first 1 h of charge at C/3 (top panel) and the normalized intensity changes, obtained by integrating over the whole active particle shown in (B) (bottom panel).

(B) Normalized differential images of the active particle during the initial charging, for the time points indicated by black circles in (A). The total contrast is shown, which represents the fractional intensity change between the current frame and the first frame of the cycle (i.e., with no current applied). The color scale is centered at zero (white), with positive values indicating an overall intensity increase (red), and negative values indicating a decrease (blue).

(C) Voltage and current profiles during the first 20 min of charge at C/3 followed by a rest period (top panel), and the normalized intensity changes of a second active particle (bottom panel).

(D) Normalized differential images of the active NMC particle during the charge-rest experiment. Scale bars, 1 μm.

properties of the NMC cathode are strongly dependent on its lithium content. Moreover, the monotonic nature of the intensity change means that intensity can be used as a qualitative proxy for the single-particle state-of-charge (SoC)/lithium content: a higher intensity corresponds to a lower lithium content. A more detailed analysis of the relationship between the optical intensity and lithium content is given in Figure S8, and the smaller changes seen above 4.1 V are shown in Figure S9.

Lithium heterogeneity at the beginning of charge

We now investigate spatially resolved delithiation and lithiation processes in single-particle NMCs. Figure 2A shows the voltage profile and intensity change during the first hour of the C/3 charge, and differential images (see experimental procedures) with respect to the beginning of the cycle at 5, 15, 25, and 35 min are shown in Figure 2B. After 5 min of delithiation at C/3, the periphery of the particle started to show a positive contrast, the higher intensity being ascribed to local NMC domains with lower lithium content (higher intensity is indicative of lower lithium content; Figure 1D). The core remains fully lithiated and a distinct lithium concentration heterogeneity inside this individual NMC particle is formed. On further charging, this periphery continued to advance toward the center of the particle, further increasing in positive contrast, while the core lagged noticeably behind (15 and 25 min, Figure 2B). After 35 min, the total contrast had become reasonably uniform across the whole particle (Video S2). We have observed this phenomenon in more than 50 different particles from seven different electrodes, confirming its reproducibility

Please cite this article in press as: Xu et al., Operando visualization of kinetically induced lithium heterogeneities in single-particle layered Ni-rich cathodes, Joule (2022), https://doi.org/10.1016/j.joule.2022.09.008

(see Figure S10). Further work on a larger set of particles is required to explore further heterogeneity effects and identify other correlations between, for example, size and shape and heterogeneity/diffusivity.

This apparent "core-shell" structure cannot be of thermodynamic origin since the (de)lithiation of Ni-rich materials is widely acknowledged to be a solid-solution process. This is in contrast to the closely related material $LiCoO_2$, which exhibits a thermodynamic two-phase region at the beginning of the charge caused by an insulator-to-metal transition, absent in NMC.[26–28] A charge-rest experiment was then performed to confirm the kinetic origin of the "core-shell" structure observed here (Figure 2C). During the ~20-min charge period, lithium heterogeneity began to develop in the particle as described above (Figure 2D). After stopping the current, however, the intensity heterogeneity across the particle gradually disappeared, and a uniform distribution was achieved by the end of the rest period (Figure 2D)—this is consistent with a kinetically driven intra-particle heterogeneity where the equilibrium state exhibits a uniform lithium distribution.

In addition to the intra-particle heterogeneity discussed above, some inter-particle reaction heterogeneity was also observed at the beginning of the charge at a higher rate of 2C (Figure S11). We ascribe this observation to differences in wiring and tortuosity of pathways for lithium transport through the bulk electrode to the NMC particles since the particles that are imaged are located the furthest from the separator (see Figure 1A and Video S3). Further studies are currently underway to quantify these effects.

Finite-element simulations and rate dependence

Guided by the experimental results, we developed a finite-element model to assist our understanding of the lithium heterogeneity observed at the beginning of the charge. Our model assumes a constant lithium flux in/out of a particle—the particle has the same cross-sectional shape as one of the particles that were examined experimentally (Figure 3A), with diffusion only occurring parallel to the basal plane of the particle. To calculate the self-diffusion coefficient, D_{Li}, of lithium inside the NMC lattice, we measured the lithium hop rate ν using solid-state NMR as a function of SoC and inferred D_{Li} from ν (see supplemental information section "ssNMR and self-diffusion coefficients").

Note that the inferred magnitude of ν depends strongly on assumptions made as part of the NMR data analysis as discussed below (supplemental information section "modeling"). Therefore, instead of directly using the value of D_{Li} inferred from the NMR hop rate data, we scaled D_{Li} by a constant factor S to obtain an effective diffusion coefficient $D_{Li}^{eff} \equiv D_{Li}/S$ while not changing the functional form of the dependence of D_{Li} on SoC. The scaling factor S was obtained by seeking for agreement between predictions of occupancy and measurements of the temporal variation of the total contrast within the NMC particle. Specifically, we assumed a linear relation between optical intensity and Li occupancy and obtained S by minimizing the root-mean-square error between the temporal intensity measurements at the center of the particle and the corresponding occupancy predictions at a charging rate of C/3. This analysis suggests $S = 3.5$ (see supplemental information and Figure S2) such that $D_{Li}^{eff} \sim 10^{-14} cm^2\ s^{-1}$ near-full lithiation. Regardless of the value of S, D_{Li}^{eff} increases by almost two orders of magnitude upon removal of 40% of the lithium (Figure 3B). Upon adopting this calibrated value of D_{Li}^{eff}, the model captures the spatio-temporal evolution of Li occupancy within the NMC particle including the

Please cite this article in press as: Xu et al., Operando visualization of kinetically induced lithium heterogeneities in single-particle layered Ni-rich cathodes, Joule (2022), https://doi.org/10.1016/j.joule.2022.09.008

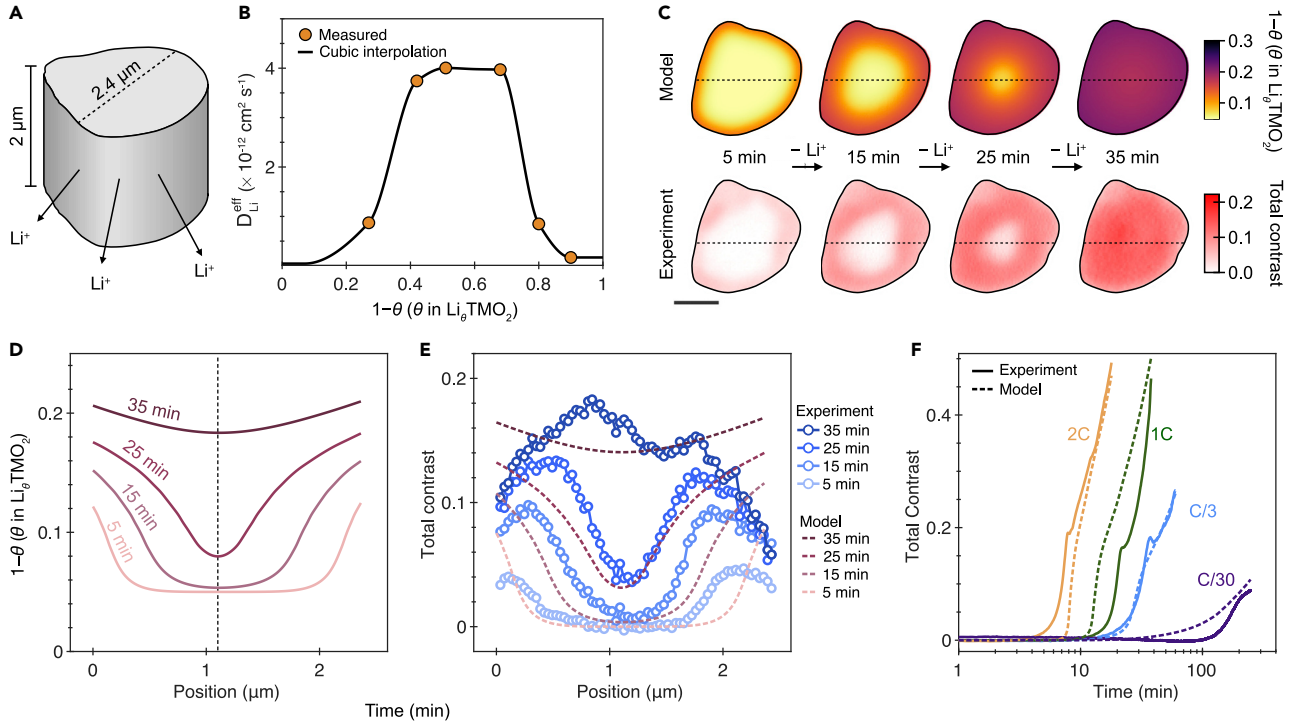

Figure 3. Comparing modeling and experiments

(A) Sketch of the particle used in the modeling.

(B) The effective lithium diffusion coefficient $D_{Li}^{eff} \equiv D_{Li}/S$ as a function of lithium content ($S = 3.5$).

(C) Comparison of simulation and experimental imaging results, both conducted at a delithiation rate of C/3. The predicted degree of delithiation ($1-\theta$) on the basal plane of the particle at various times during the charge.

(D and E) Evolution of (D) the degree of delithiation in the simulation and (E) the total contrast in the optical images along the horizontal dotted line marked in (C). In (E), we include the corresponding predictions (shown with dashed curves) of the total contrast.

(F) Evolution of measurements and predictions of total contrast at the center of the particle (shown by the vertical dashed lines in D).

development of sharp concentration gradients during delithiation at C/3 (Figures 3C–3E). These spatial heterogeneities occur over a wide range of charging rates, and the model reproduces these observations for charging rates ranging from C/30 to 2C (Figures S12 and S13).

The lithium heterogeneity during charging can be succinctly illustrated by retrieving the lithium content at the center of the particle (Figure 3F). Again, the model is in good agreement with experimental results and clearly shows that the delithiation of the particle center lags noticeably behind the surface at the start of the CC charge at all charging rates, indicating that the delithiation front takes significant time to reach the center. Our model also indicates that the intra-particle heterogeneity is strongly dependent on the particle size, i.e., smaller particles show less pronounced heterogeneity (Figures S14 and S15), which is in good agreement with the experiment (Figure S16; Video S4). We note that our modeling revealed that some spatial lithium-ion heterogeneity can also arise when the ion diffusivity is assumed to be constant but small in magnitude and below 5×10^{-14} cm^2 s^{-1}, see Figure S17D. However, the temporal evolution of the ion concentration assuming a constant diffusivity fails to capture the delayed response of the particle center followed by a quick delithiation (Figure S17) as seen in the experimentally observed intensity measurements (Figure 3F). Taken together, these results strongly support our hypothesis that the observed heterogeneous delithiation is consistent with a strong sensitivity of diffusivity to lithium content at the beginning of the charge.

Please cite this article in press as: Xu et al., Operando visualization of kinetically induced lithium heterogeneities in single-particle layered Ni-rich cathodes, Joule (2022), https://doi.org/10.1016/j.joule.2022.09.008

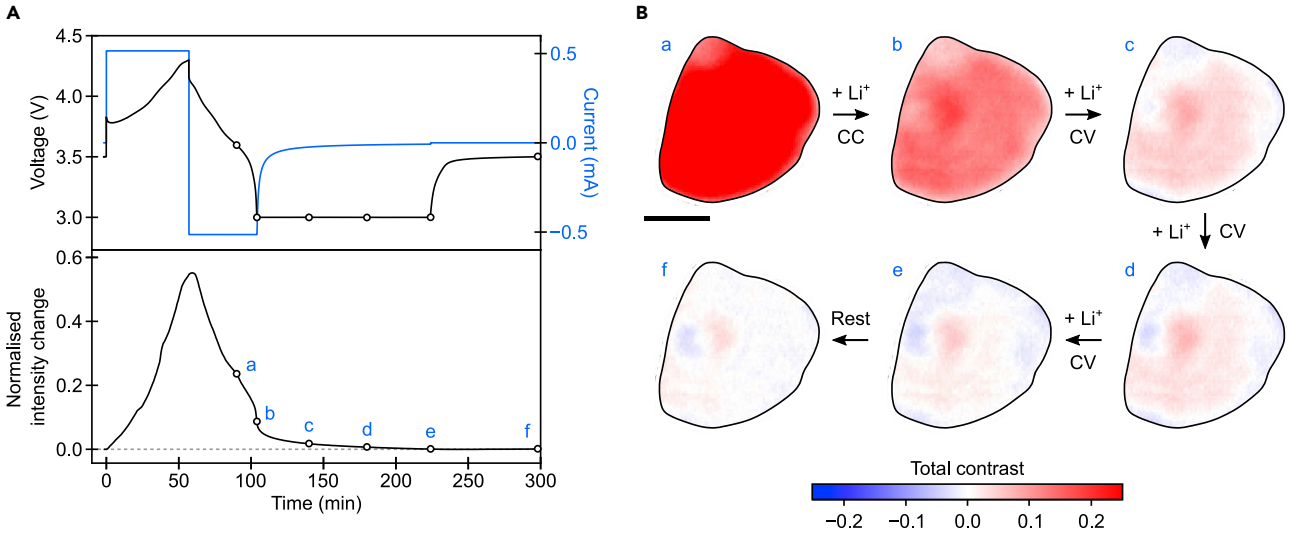

Figure 4. Lithium heterogeneity at the end of discharge

(A) Voltage and current profile (top panel) and normalized intensity changes of the active particle during a 1C rate CC charge and CCCV discharge cycle. CV was performed at 3 V for 2 h. The dashed gray line (bottom panel) is a guide for the eye, representing 0 intensity change. The initial lithium content is estimated to be ~97% based on the open circuit voltage (OCV, ~3.5 V versus Li/Li$^+$). Note that this near-full lithiation state was achieved by applying a 2-h voltage hold at 3 V after the end of CC discharge in the previous cycle.

(B) Differential images of an NMC active particle during the discharge, at the times indicated by black circles in (A) (where a, b, c, d, e, and f are at 90, 104, 140, 180, 224, and 298 min, respectively). Scale bars, 1 μm. The current at the end of the CV period was −7.59 μA (equivalent to ~C/200; a negative sign denotes discharging current).

Lithium heterogeneity at the end of discharge

We next explored in more detail how these dynamic lithium heterogeneities influence the first-cycle capacity loss in layered Ni-rich materials. During CC cycling at 1C (Figure 4A), the normalized intensity of the particle followed the same trends as seen above. Importantly, however, at the end of discharge, the particle intensity was 8% higher than its initial value, indicating incomplete reinsertion of lithium, in line with the voltage-capacity profile (Figure S18). During a subsequent 2-h CV hold at 3 V, an extra capacity of ~24 mA h g^{-1} could be extracted (increasing the CE from 82.3% to 94.3%), and the mean intensity reached its initial value.

Examining the spatial intensity variations across the particle shows that the intensity of the active particle remained uniform for the first 30 min of the 1C discharge (a in Figure 4B). At the end of the CC discharge (104 min, b in Figure 4B), the vast majority of the particle still exhibited a lower lithium content (positive total contrast, red) compared with the beginning of the charge. Yet, around a narrow periphery of the particle, the total contrast was close to zero (Figure S18), indicating that the particle has a lithium-rich periphery (with the lithium content approaching that of the particle before charging) and a more lithium-deficient core. The fact that the core remains lithium deficient can be explained by the drastically reduced lithium diffusion coefficient at near-full lithiation states (Figure S19).[11,14] For occupancy of $(1-\theta) < 0.2$, the drop in diffusivity produces a significant concentration gradient across the particle, which is more pronounced at faster-charging rates (Figure S19).

With the additional CV step, the particle was re-lithiated further as indicated by the continued decrease in total contrast (c, d, and e in Figure 4B). In particular, a large fraction of the particle returned to the initial intensity (~0 total contrast, white). At the end of the CV step (e in Figure 4B), the variation in the contrast (hence the lithium

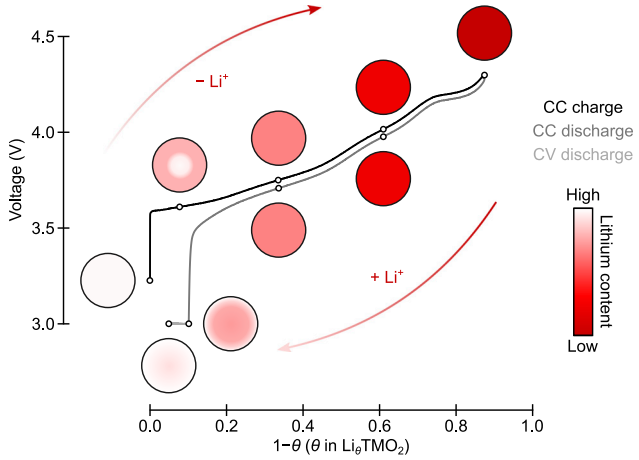

Figure 5. Summary of the lithium-ion distribution within the single active particle at various lithium contents

The circles show schematic representations of single-particle Ni-rich materials at various SoCs. The voltage profile is illustrative of the single-crystal NMC material used in this work and was obtained in a half-cell cycled with a CC charge and CC discharge (C/20 rate) and a discharge CV hold at 3 V (for 24 h).

content) across the particle becomes very small, and further equilibration is seen after the open circuit voltage (OCV) rest (f in Figure 4B). These results confirm that the capacity loss induced by the kinetic limitations mentioned above can be, to a large extent, recovered by a slow lithiation step. Note that even with a very long voltage hold at the end of discharge, the first-cycle CE still does not reach 100%, as demonstrated here (Figure 5) and in other studies in the literature.[5,13,29] The CE of coin cells is, however, significantly higher, and the poorer CE in the optical experiments is attributed to the unconventional cell setup (see Figures S6 and S7). The remaining first-cycle loss is attributed to electrolyte degradation at high voltages and mechanisms associated with a loss of active material due to, for instance, transition metal dissolution[30–32] and surface reconstruction.[33–35] Consistent with this, the CE increases as the rate increases approaching 98% at 2C (see Figure S6), the electrodes spending less time at higher voltages. Given the extremely low diffusivity of the fully lithiated material with no Li vacancies, it is also possible that not all of the particles in the whole electrode are fully lithiated even after the long hold.

DISCUSSION

Lithium heterogeneities during delithiation and lithiation

When delithiating the layered cathodes from full (and near-full) lithiation states, a noticeable lithium heterogeneity is seen with a lithium-rich core and a lithium-poor periphery (summarized in Figure 5). The SoC range during which this heterogeneity is present is dependent on the initial state of charge as well as the charging rate. This lithium heterogeneity arises from the low lithium diffusivity at near-full lithiation, which is insufficient to support a high lithium-ion flux uniformly throughout the particle. Instead, as the lithium is extracted from the periphery of the particle, the periphery develops a higher lithium diffusivity due to its lower lithium occupancy, accelerating the rate of lithium-ion extraction from the lithium-poor periphery domains further. Simultaneously, the boundary between the lithium-rich and lithium-poor domains propagates toward the center of the particle as the charging progresses, until the particle becomes uniform in lithium content, and no obvious heterogeneity occurs during the rest of the charging.

Please cite this article in press as: Xu et al., Operando visualization of kinetically induced lithium heterogeneities in single-particle layered Ni-rich cathodes, Joule (2022), https://doi.org/10.1016/j.joule.2022.09.008

During CV discharge, lithium insertion occurs predominantly uniformly throughout the particle, except at the very end where a narrow periphery becomes notably lithium-rich compared with the core. This results from two kinetic limitations, slow lithium diffusion—seen by ssNMR measurements—and slow charge transfer kinetics (see potentiostatic intermittent titration results in Figure S20), both of which lead to a substantial increase in the over-potential and hence a steep decrease in the cell voltage during CC discharge. As a result, the cell quickly reaches the cut-off voltage with the core of the NMC particles in a lithium-deficient state and therefore causes a capacity loss. Such kinetic limitations can be largely overcome by a much slower lithiation process, for instance, by inserting a CV hold at 3 V versus Li/Li^+ in the present case. Although the degree of heterogeneity at the end of discharge is much less significant than that seen at the beginning of the charge, it is nonetheless capable of resulting in a loss in capacity of as much as 10% when using standard CC cycling regimes.

Lithium heterogeneity in related NCA materials at the beginning of the first charge was proposed recently by Grenier et al.,[13] in the SoC range of $0.96 > \theta > 0.74$ on the basis of *operando* synchrotron powder XRD. Here, the XRD pattern was modeled with two different phases, with the difference in lithium content between the lithium-poor and the lithium-rich phase gradually increasing from 0.09 at $\theta = 0.96$ to 0.18 at $\theta = 0.74$—such lithium heterogeneity was ascribed to be intra-particle. XRD, however, is a bulk technique and provides no spatially resolved information. Conversely, Park et al. recently suggested, on the basis of *ex situ* X-ray absorption microscopy experiments, that this heterogeneity occurs between, rather than within, particles.[14] They proposed an intrinsic mechanism for the apparent phase separation observed during the delithiation of NMC, termed "electro-autocatalysis," which describes the increase in the interfacial exchange current density as lithium content decreases.[14]

Our work expands on these studies, directly demonstrating that both proposed mechanisms will be at play under operating conditions. Critically, the intra-particle heterogeneity observed in our work cannot be captured by *ex situ* experiments (see Figure 2D). We further note that non-uniform lithiation during the CC and CV discharge has not been previously seen by XRD,[13] presumably because it represented a very small fraction of the bulk, highlighting the unique capability of our optical imaging technique to capture the transient and small heterogeneities in battery materials.

A scaling factor of 3.5 was needed to reconcile the NMR-derived diffusivities and those predicted on the basis of the finite-element modeling. This is (as discussed in the supplemental information) ascribed to the errors implicit in the extraction of NMR hop rates in the NMR experiment, where we used the NMR-derived maximum hopping rate and did not include the distributions of correlation times seen experimentally, nor the nature of the hops of the Li^+ ions in between the NMC layers. The diffusivities extracted from the simulations represent the effective diffusivities on a 2D lattice during cycling. Future experiments and simulations will explore how these vary from particle to particle and as a function of transition metal content in the NMC material.

Practical implications

The lithium heterogeneity at the beginning of the charge will generate a noticeable difference in lattice constants between the lithium-rich and lithium-poor domains. At fast C-rates, for instance, 1C and 2C, the SoC difference between the periphery and the core can be as large as 20%–30% within a narrow length scale based on our modeling (Figure S13). This large concentration gradient will lead to internal stress/strain within individual particles, which may further result in mechanical degradation such as particle fracturing, especially for larger particle sizes. Moreover, the first-cycle CE loss is of

particular importance since it reduces the energy density of practical cells: although graphite anode performances have been continuously improved with the first-cycle CEs now approaching 96%,[36] that of the Ni-rich materials is limited to ~90%. Therefore, increasing the first-cycle efficiency of the cathode can lead to a direct increase in the reversible energy density at the cell level. Such an increase will be more evident for the next generation of high-energy-density batteries consisting of a Ni-rich cathode and a lithium metal anode. Our results show that the key to improving performance lies in increasing the lithium mobility and charge transfer kinetics at near-full lithiation states. Although current literature is yet inconclusive as to what may be the most effective approaches to improve the first-cycle CE, certain coating materials—for instance, Nb-containing compounds[37]—have been shown to be promising.

Concluding remarks

In this work, we employed *operando* optical microscopy to track the lithium-ion dynamics in single-particle layered Ni-rich NMC, with a particular focus on understanding the transient lithium heterogeneities at the single-particle scale. The observed optical intensity revealed a substantial increase upon delithiation (charge) and a decrease upon lithiation (discharge), indicating that the optical intensity can be used as a qualitative probe for the local lithium content.

The spatially resolved intensity changes showed clear lithium heterogeneity at the beginning of the charge, exhibiting particles with a lithium-poor periphery and lithium-rich core. This intra-particle heterogeneity persisted across a wide range of C-rates, from C/30 to 2C. By developing a finite-element model, we demonstrated that this phenomenon is due to a kinetic diffusion-driven mechanism, caused by low lithium diffusivity at near-full lithiation states, which increases dramatically on delithiation. Combining the optical results with ssNMR and modeling, we extracted accurate values for the concentration-dependent lithium-ion diffusion coefficient of the Ni-rich NMC cathode material under study.

We further showed that when approaching high lithiation states on discharge, the NMC particle surface gradually becomes saturated by lithium due to the decreased lithium diffusivity at high lithiation states. Coupled with slow charge transfer kinetics, this is one of the main reasons for the first-cycle Coulombic inefficiency of layered Ni-rich materials. These results pave the way toward a better understanding of possible improvements in current state-of-the-art NMC materials and more broadly highlight the importance of understanding nanoscale dynamic changes in battery materials during their operation.

EXPERIMENTAL PROCEDURES

Resource availability

Lead contact

Further information and requests for resources should be directed to and will be fulfilled by the lead contact, Clare P. Grey (cpg27@cam.ac.uk).

Materials availability

This study did not generate new unique reagents.

Data and code availability

The data supporting the findings of this study are available within the main text and the supplemental information. More detailed data and the code for simulation can be made available upon request to the corresponding author.

Full experimental procedures are provided in the supplemental information.

SUPPLEMENTAL INFORMATION

Supplemental information can be found online at https://doi.org/10.1016/j.joule.2022.09.008.

ACKNOWLEDGMENTS

The authors are grateful to Umicore for providing the NMC material used in this work and to Dr. Jérémie Auvergniot for helpful discussions. We thank Dr. Katharina Märker for her help with the NMR experiments and simulations. This work was supported by the Faraday Institution Degradation Project (grant numbers FIRG001 and FIRG024). A.J.M. acknowledges support from the EPSRC Cambridge NanoDTC, EP/L015978/1. C.S. acknowledges financial support from the Royal Commission of the Exhibition of 1851. A.R. acknowledges financial support from the EPSRC and the Winton Program for the Physics of Sustainability. This project has received funding from the European Research Council (ERC) under the European Union's Horizon 2020 research and innovation programme (grant agreement no. 758826). N.A.F. acknowledges funding from the European Research Council in the form of an advanced grant (MULTILAT, 669764). C.P.G. acknowledges support from an ERC Advanced Investigator Grant (EC H2020 ERC 835073).

AUTHOR CONTRIBUTIONS

C.P.G., A.R., and C.S. conceived the idea of this work. C.X., A.J.M., Z.L., and C.S. performed the *operando* optical microscopy experiments. C.X. analyzed the optical microscopy data with support from A.J.M., Z.L., and C.S. C.X. performed electrochemical characterizations and SEM and analyzed the data. Z.L. performed XRD. C.X. performed the Rietveld Refinement. D.S.H. performed ssNMR measurements and analyzed data. S.S.P. developed the model and carried out finite-element simulations under the guidance of N.A.F. and V.S.D. All authors discussed the results and contributed to the manuscript writing.

DECLARATION OF INTERESTS

A.J.M., C.S., A.R., and C.P.G. are founders of Illumion, Ltd.

INCLUSION AND DIVERSITY

We support the inclusive, diverse, and equitable conduct of research.

Received: February 10, 2022
Revised: April 4, 2022
Accepted: September 20, 2022
Published: October 12, 2022

REFERENCES

1. Blomgren, G.E. (2017). The development and future of lithium ion batteries. J. Electrochem. Soc. *164*, A5019–A5025. https://doi.org/10.1149/2.0251701jes.

2. Li, W., Erickson, E.M., and Manthiram, A. (2020). High-nickel layered oxide cathodes for lithium-based automotive batteries. Nat. Energy *5*, 26–34. https://doi.org/10.1038/s41560-019-0513-0.

3. Choi, J.U., Voronina, N., Sun, Y.-K., and Myung, S.-T. (2020). Recent progress and perspective of advanced high-energy Co-Less Ni-Rich cathodes for Li-ion batteries: yesterday, today, and tomorrow. Adv. Energy Mater. *10*, 2002027. https://doi.org/10.1002/aenm.202002027.

4. Grey, C.P., and Hall, D.S. (2020). Prospects for lithium-ion batteries and beyond—a 2030 vision. Nat. Commun. *11*, 6279. https://doi.org/10.1038/s41467-020-19991-4.

5. Zhou, H., Xin, F., Pei, B., and Whittingham, M.S. (2019). What limits the capacity of layered oxide cathodes in lithium batteries? ACS Energy Lett. *4*, 1902–1906. https://doi.org/10.1021/acsenergylett.9b01236.

6. Xie, Q., Li, W., and Manthiram, A. (2019). A Mg-doped high-nickel layered oxide cathode enabling safer, high-energy-density Li-ion batteries. Chem. Mater. *31*, 938–946. https://doi.org/10.1021/acs.chemmater.8b03900.

7. Kim, U.-H., Park, G.-T., Son, B.-K., Nam, G.W., Liu, J., Kuo, L.-Y., Kaghazchi, P., Yoon, C.S., and Sun, Y.-K. (2020). Heuristic solution for achieving long-term cycle stability for Ni-rich layered cathodes at full depth of discharge. Nat. Energy *5*, 860–869. https://doi.org/10.1038/s41560-020-00693-6.

8. Li, W., Liu, X., Celio, H., Smith, P., Dolocan, A., Chi, M., and Manthiram, A. (2018). Mn versus Al in Layered Oxide Cathodes in lithium-Ion Batteries: A Comprehensive Evaluation on Long-Term Cyclability. Adv. Energy Mater. *8*, 1703154. https://doi.org/10.1002/aenm.201703154.

9. Ryu, H.-H., Namkoong, B., Kim, J.-H., Belharouak, I., Yoon, C.S., and Sun, Y.-K. (2021). Capacity fading mechanisms in Ni-Rich Single-Crystal NCM cathodes. ACS Energy Lett. *6*, 2726–2734. https://doi.org/10.1021/acsenergylett.1c01089.

10. Märker, K., Xu, C., and Grey, C.P. (2020). Operando NMR of NMC811/graphite lithium-ion batteries: structure, dynamics, and lithium metal deposition. J. Am. Chem. Soc. *142*, 17447–17456. https://doi.org/10.1021/jacs.0c06727.

11. Ge, M., Wi, S., Liu, X., Bai, J., Ehrlich, S., Lu, D., Lee, W.K., Chen, Z., and Wang, F. (2021). Kinetic limitations in single-crystal high-nickel cathodes. Angew. Chem. Int. Ed. Engl. *60*, 17350–17355. https://doi.org/10.1002/anie.202012773.

12. Grenier, A., Liu, H., Wiaderek, K.M., Lebens-Higgins, Z.W., Borkiewicz, O.J., Piper, L.F.J., Chupas, P.J., and Chapman, K.W. (2017). Reaction heterogeneity in $LiNi_{0.8}Co_{0.15}Al_{0.05}O_2$ induced by surface layer. Chem. Mater. *29*, 7345–7352. https://doi.org/10.1021/acs.chemmater.7b02236.

13. Grenier, A., Reeves, P.J., Liu, H., Seymour, I.D., Märker, K., Wiaderek, K.M., Chupas, P.J., Grey, C.P., and Chapman, K.W. (2020). Intrinsic kinetic limitations in substituted lithium-layered transition-metal oxide electrodes. J. Am. Chem. Soc. *142*, 7001–7011. https://doi.org/10.1021/jacs.9b13551.

14. Park, J., Zhao, H., Kang, S.D., Lim, K., Chen, C.C., Yu, Y.S., Braatz, R.D., Shapiro, D.A., Hong, J., Toney, M.F., et al. (2021). Fictitious phase separation in Li layered oxides driven by electro-autocatalysis. Nat. Mater. *20*, 991–999. https://doi.org/10.1038/s41563-021-00936-1.

15. Xu, C., Märker, K., Lee, J., Mahadevegowda, A., Reeves, P.J., Day, S.J., Groh, M.F., Emge, S.P., Ducati, C., Layla Mehdi, B., et al. (2021). Bulk fatigue induced by surface reconstruction in layered Ni-rich cathodes for Li-ion batteries. Nat. Mater. *20*, 84–92. https://doi.org/10.1038/s41563-020-0767-8.

16. Märker, K., Reeves, P.J., Xu, C., Griffith, K.J., and Grey, C.P. (2019). Evolution of structure and lithium dynamics in $LiNi_{0.8}Mn_{0.1}Co_{0.1}O_2$ (NMC811) cathodes during electrochemical cycling. Chem. Mater. *31*, 2545–2554. https://doi.org/10.1021/acs.chemmater.9b00140.

17. Xu, C., Reeves, P.J., Jacquet, Q., and Grey, C.P. (2021). Phase behavior during electrochemical cycling of Ni-Rich cathode materials for Li-ion batteries. Adv. Energy Mater. *11*, 2003404. https://doi.org/10.1002/aenm.202003404.

18. Tian, C., Xu, Y., Nordlund, D., Lin, F., Liu, J., Sun, Z., Liu, Y., and Doeff, M. (2018). Charge heterogeneity and surface chemistry in polycrystalline cathode materials. Joule *2*, 464–477. https://doi.org/10.1016/j.joule.2017.12.008.

19. Cao, C., Toney, M.F., Sham, T.-K., Harder, R., Shearing, P.R., Xiao, X., and Wang, J. (2020). Emerging X-ray imaging technologies for energy materials. Mater. Today *34*, 132–147. https://doi.org/10.1016/j.mattod.2019.08.011.

20. Lu, J., Wu, T., and Amine, K. (2017). State-of-the-art characterization techniques for advanced lithium-ion batteries. Nat. Energy *2*, 17011. https://doi.org/10.1038/nenergy.2017.11.

21. Martens, I., Melo, L.G.A., Wilkinson, D.P., Bizzotto, D., and Hitchcock, A.P. (2019). Characterization of X-ray damage to perfluorosulfonic acid using correlative microscopy. J. Phys. Chem. C *123*, 16023–16033. https://doi.org/10.1021/acs.jpcc.9b03924.

22. Merryweather, A.J., Schnedermann, C., Jacquet, Q., Grey, C.P., and Rao, A. (2021). Operando optical tracking of single-particle ion dynamics in batteries. Nature *594*, 522–528. https://doi.org/10.1038/s41586-021-03584-2.

23. Ortega-Arroyo, J., and Kukura, P. (2012). Interferometric scattering microscopy (iSCAT): new frontiers in ultrafast and ultrasensitive optical microscopy. Phys. Chem. Chem. Phys. *14*, 15625–15636. https://doi.org/10.1039/c2cp41013c.

24. Piliarik, M., and Sandoghdar, V. (2014). Direct optical sensing of single unlabelled proteins and super-resolution imaging of their binding sites. Nat. Commun. *5*, 4495. https://doi.org/10.1038/ncomms5495.

25. Gholami Mahmoodabadi, R., Taylor, R.W., Kaller, M., Spindler, S., Mazaheri, M., Kasaian, K., and Sandoghdar, V. (2020). Point spread function in interferometric scattering microscopy (iSCAT). Part I: aberrations in defocusing and axial localization. Opt. Express *28*, 25969–25988. https://doi.org/10.1364/OE.401374.

26. Marianetti, C.A., Kotliar, G., and Ceder, G. (2004). A first-order Mott transition in Li_xCoO_2. Nat. Mater. *3*, 627–631. https://doi.org/10.1038/nmat1178.

27. Ménétrier, M., Carlier, D., Blangero, M., and Delmas, C. (2008). On "really" stoichiometric $LiCoO_2$. Electrochem. Solid State Lett. *11*, A179. https://doi.org/10.1149/1.2968953.

28. Ménétrier, M., Saadoune, I., Levasseur, S., and Delmas, C. (1999). The insulator-metal transition upon lithium deintercalation from $LiCoO_2$: electronic properties and ^7Li NMR study. J. Mater. Chem. *9*, 1135–1140. https://doi.org/10.1039/A900016J.

29. Seidlmayer, S., Buchberger, I., Reiner, M., Gigl, T., Gilles, R., Gasteiger, H.A., and Hugenschmidt, C. (2016). First-cycle defect evolution of $Li_{1-x}Ni_{1/3}Mn_{1/3}Co_{1/3}O_2$ lithium ion battery electrodes investigated by positron annihilation spectroscopy. J. Power Sources *336*, 224–230. https://doi.org/10.1016/j.jpowsour.2016.10.050.

30. Wandt, J., Freiberg, A., Thomas, R., Gorlin, Y., Siebel, A., Jung, R., Gasteiger, H.A., and Tromp, M. (2016). Transition metal dissolution and deposition in Li-ion batteries investigated by operando X-ray absorption spectroscopy. J. Mater. Chem. A *4*, 18300–18305. https://doi.org/10.1039/C6TA08865A.

31. Zhan, C., Wu, T., Lu, J., and Amine, K. (2018). Dissolution, migration, and deposition of transition metal ions in Li-ion batteries exemplified by Mn-based cathodes – a critical review. Energy Environ. Sci. *11*, 243–257. https://doi.org/10.1039/C7EE03122J.

32. Ruff, Z., Xu, C., and Grey, C.P. (2021). Transition metal dissolution and degradation in NMC811-graphite electrochemical cells. J. Electrochem. Soc. *168*, 060518. https://doi.org/10.1149/1945-7111/ac0359.

33. Lin, F., Markus, I.M., Nordlund, D., Weng, T.-C., Asta, M.D., Xin, H.L., and Doeff, M.M. (2014). Surface reconstruction and chemical evolution of stoichiometric layered cathode materials for lithium-ion batteries. Nat. Commun. *5*, 3529. https://doi.org/10.1038/ncomms4529.

34. Streich, D., Erk, C., Guéguen, A., Müller, P., Chesneau, F.-F., and Berg, E.J. (2017). Operando monitoring of early Ni-mediated surface reconstruction in layered lithiated Ni–Co–Mn oxides. J. Phys. Chem. C *121*, 13481–13486. https://doi.org/10.1021/acs.jpcc.7b02303.

35. Li, L., Self, E.C., Darbar, D., Zou, L., Bhattacharya, I., Wang, D., Nanda, J., and Wang, C. (2020). Hidden subsurface reconstruction and its atomic origins in layered oxide cathodes. Nano Lett. *20*, 2756–2762. https://doi.org/10.1021/acs.nanolett.0c00380.

36. Asenbauer, J., Eisenmann, T., Kuenzel, M., Kazzazi, A., Chen, Z., and Bresser, D. (2020). The success story of graphite as a lithium-ion anode material – fundamentals, remaining challenges, and recent developments including silicon (oxide) composites. Sustainable Energy Fuels *4*, 5387–5416. https://doi.org/10.1039/D0SE00175A.

37. Xin, F., Zhou, H., Zong, Y., Zuba, M., Chen, Y., Chernova, N.A., Bai, J., Pei, B., Goel, A., Rana, J., et al. (2021). What is the role of Nb in nickel-rich layered oxide cathodes for lithium-ion batteries? ACS Energy Lett. 1377–1382. https://doi.org/10.1021/acsenergylett.1c00190.

Joule, Volume *6*

Supplemental information

Operando visualization of kinetically induced lithium heterogeneities in single-particle layered Ni-rich cathodes

Chao Xu, Alice J. Merryweather, Shrinidhi S. Pandurangi, Zhengyan Lun, David S. Hall, Vikram S. Deshpande, Norman A. Fleck, Christoph Schnedermann, Akshay Rao, and Clare P. Grey

EXPERIMENTAL PROCEDURES

Materials and battery preparation

The monolithic NMC cathode material (nominal composition: $LiNi_{0.87}Mn_{0.05}Co_{0.08}O_2$) used in this work was kindly provided by Umicore. Self-standing electrodes consisted of the NMC active material, SuperP Li carbon black and polytetrafluoroethylene (PTFE) binder in a mass ratio of 70:25:5. NMC powder and SuperP Li carbon were first mixed using a Thinky mixer at 2000 rpm for 5 minutes in a sealed container, and PTFE dry powder was added, and all three powders were mixed at 2000 rpm for another 5 minutes. Note these two mixing steps were both performed in dry conditions and no solvents were involved. After mixing, the mixture was gently ground using a mortar and pestle until it aggregated into small patches, then it was further pressed and rolled into thin and flexible films. Circular electrodes with a typical diameter of 6 mm were punched out and dried at 120 ºC for 12 hours under a dynamic vacuum (low 10^{-2} mbar). Self-standing electrodes had been prepared in an Argon glovebox to ensure minimum contact with air. All the weighing was done inside the glovebox and the powder was sealed in a container which was taken out from the glovebox for mixing and transferred back for further weighing and processing (i.e., grinding and rolling). Note the carbon black used for the electrodes prepared in the glovebox was pre-dried at 120 ºC under dynamic vacuum (low 10^{-2} mbar) to remove moisture contamination.

Conventional laminate electrodes were prepared by mixing the same NMC material with SuperP Li and Kynar HSV900 poly(vinylidene fluoride) (PVDF) binder in a mass ratio of 90:5:5, and an adequate amount of 1-methyl-2-pyrrolidinone (NMP) solvent. The mixing was performed at 2000 rpm for a total of 10 minutes (5 minutes, two times). The obtained slurry was cast onto an Al foil (battery grade, 20 μm) and the wet electrode sheet was then pre-dried at ~80 ºC to remove the NMP solvent under dry N_2 flow (to avoid the NMC material reacting with air). The pre-dried laminate electrode sheet was then punched into circular disks (typically in 13 mm diameter), which were further dried at 120 ºC for 12 hours under dynamic vacuum (low 10^{-2} mbar).

Batteries: Two cell formats, standard coin cells and optical cells, have been used in this work. All cells were made with one NMC electrode as the cathode, one lithium metal disk as the anode (i.e. half cells), one piece of GF-B separator and adequate amount of the LP30 electrolyte (1 M $LiPF_6$, ethylene carbonate/dimethyl carbonate (EC:DMC), 1/1). Cells were assembled in a dry argon atmosphere.

The optical cell (see Figure 1A) is based on a commercially available model (EL-CELL, ECC-Opto-Std test cell), with a homemade lid that was designed to be compatible with our microscope objective and glass observation windows (thickness 170 μm). The working electrode consisted of the self-standing NMC film, with an aluminium mesh current collector pressed on top, contacted via a stainless-steel pin. The LP30 electrolyte was injected into the cell following assembly of the electrode stack. Rubber O-rings ensured that the cell remained adequately air-tight during the optical measurements.

Physical characterisations

Scanning electron microscopy (SEM) experiments were performed on the self-standing electrodes using a TESCAN MIRA3 FEG-SEM at 5.0 kV with In-Beam secondary electron detection. Powder X-ray diffraction (PXRD) experiments were carried out on an X'pert diffractometer at 298 K from 5º to 100º (2θ range) using Cu–Kα radiation (L = 154.06 pm, 154.43 pm) in the Bragg–Brentano geometry, with a step size of 0.01671º and a step time of 85.09 seconds.

Electrochemistry

Typical galvanostatic cycling (CC charge and CC discharge) were carried out between 3 V and 4.3 V at various rates (C/30, C/3, 1C or 2 C, where the C-rate is defined using a practical capacity of 210 mA h g^{-1}). For certain cycles, an additional two-hour voltage hold at 3 V was applied after the CC discharge. GITT experiments were performed using a 15 min constant current pulse (current density was equivalent to C/20), followed by 4 h rest.

Optical microscopy

Optical setup. Optical scattering microscopy was carried out using an adapted version of our previously described microscope setup.[1] Briefly, a home-built inverted interferometric scattering microscope equipped with an oil immersion objective (100×, UPLSAPO100XO, Olympus) and polarisation optics in the detection path imaged the reflected and scattered light from the sample onto a CMOS detector (FLIR, Grashopper3, GS3-U3-23S6M-C) with an overall magnification of 166.7× (effective pixel size of 34.7 nm px^{-1}). In this work, the sample was illuminated at 740 nm by an LED source (Thorlabs SOLIS), equipped with a ground glass diffuser to minimise speckle contributions and homogenise the illumination.[2] The field of view was controlled by a field aperture and set to achieve a circular illumination profile with a diameter of 35 µm. Note that the probing depth of this technique with the red LED source is estimated to be ~200 nm based on the refractive index of $LiCoO_2$.[1]

The optical cell was mounted on an XYZ nano-positioner stack (Attocube, ECSx5050/AL/RT/NUM) with an overall travel range of 30 mm in all dimensions. During measurements, the sample focus position was maintained to within ±4 nm via an active external focus stabilisation based on a calibrated line-reflection profile of a 980 nm reference laser, as described previously.[1] The lateral imaging resolution in our setup is diffraction-limited to 265 nm, with a nominal depth of field of ~300 nm. Critically, the high signal-to-noise ratio of the technique can afford an excellent lateral localisation precision of sub-5 nm.[1]

Data acquisition. Optical scattering studies were carried out using a range of data acquisition parameters. Images were acquired with camera exposure times ranging from 1.8 to 3.5 ms, at a consistent frame rate of 10 Hz. Sets of recorded images were temporally binned together, with the number of binned frames ranging from 20 to 100, yielding effective frame rates of 1/2 to 1/10 Hz.

Note that all timestamps in the presented results are defined such that the beginning of each charge-discharge cycle starts at 0 min (*i.e*. excluding rest periods).

Image processing

Drift correction. All recorded image stacks were first corrected for stage drift in the *xy*-plane by isolating a bright sub-diffraction limited spot in the image (unrelated to the active particle) and fitting its position over time using a two-dimensional Gaussian function. The extracted centre positions in *x* and *y* for each image were subsequently used to correct for stage drift.

Differential image analysis. To visualize the changes in the image throughout cycling, we performed a differential background normalisation by subtracting the first frame from the k^{th} frame and then normalised by the first frame (see Equation 1). The resulting image contrast describes that fractional intensity change with respect to the initial frame (with the scale centred around 0) and is denoted as 'total contrast' in this work:

$$\text{total contrast} = \frac{I_k - I_0}{I_0} = \frac{I_k}{I_0} - 1, \qquad [1]$$

Where I_k is the intensity of the k^{th} frame and I_0 is the intensity of the first frame before any charging/discharging. We note that the same results are obtained by a background subtraction ($I_k - I_0$), albeit at different absolute intensity.

Masking. The differential images were additionally masked for clarity to exclude regions that are not part of the active particle. To accomplish this, binary masks were defined with an intensity threshold in the first frame of the cycle. Pixels with intensities below the threshold were recognized as background and their values were set to 0.

Normalised intensity change values (plotted in Figures 1E, 2A, 2C, 4A, S8, S9A, S10A, S10C, S10E, S11, S18) were obtained by integrating the total contrast values over an entire active particle.

Solid-state Nuclear Magnetic Resonance (ssNMR) Spectroscopy

Solid-state ^{7}Li MAS-NMR experiments were performed following the methods of Märker *et al*.[3] Measurements were collected with a 4.7 T (200 MHz ^{1}H Larmor frequency) Bruker Avance III spectrometer, using a Bruker 1.3 mm double-resonance probe. ^{7}Li radiofrequency (rf) pulses were applied at ~230 kHz field strength. All spectra were acquired at a magic-angle spinning (MAS) frequency of 60 kHz. Saturation-recovery experiments were used to measure spin-lattice T_1 relaxation times of the bulk NMC signal (but not the signals from the diamagnetic Li salts at

~0 ppm), which varied between ~4.6 – 8.5 ms. Recycle delays were set to 5 × T_1 (*i.e.*, ~23 – 43 ms). ^{7}Li chemical shifts were referenced externally to Li_2CO_3 (0 ppm).

NMC samples at various SoCs were prepared by charging NMC/Li half cells using a constant-current constant-voltage (CCCV) protocol, at a nominal rate of C/20 (at 4.3 V vs Li/Li$^+$) followed by a 20 h voltage hold. The cells were transferred to an argon-filled glovebox and opened. The positive electrodes were gently rinsed three times with DMC (3 × ~0.5 mL), allowed to dry, and then the NMC/binder composites were scraped off the Al current collector with a stainless-steel spatula. The materials were packed into 1.3 mm MAS-NMR rotors.

For projection magic-angle turning phase-adjusted sideband separation (MATPASS)[4] spectra, eight t_1 (time) increments were recorded. The number of transients acquired per t_1 increment was varied between 10,240 – 102,400 depending on the S/N intensity ratio, which depended on the Li content (*i.e.*, the SOC), of each sample. Two-dimensional spectra were processed using the 'tilt' (shear) and 'proj' (calculate sum) commands in TopSpin 4.0.7, to produce the one-dimensional spectra presented in this work.

Supplementary Section 1: Modelling

We consider a single prismatic single-crystal NMC particle within a composite cathode, such that the NMC particle is surrounded by the electrolyte and remains electrically neutral (as it is connected to the current collector via the carbon binder within the cathode). We introduce Cartesian coordinates x_i ($i = 1,2,3$), along with an orthonormal set of base vectors $\boldsymbol{e}_i$ such that $\boldsymbol{e}_1$ and $\boldsymbol{e}_2$ are aligned with the crystal $\boldsymbol{a}$ and $\boldsymbol{b}$ axes (that lie in the basal plane of the NMC crystal), while $\boldsymbol{e}_3$ is along the crystal $\boldsymbol{c}$ axis. The position vector of a material point within the particle is given by $\mathbf{x} = x_i\mathbf{e}_i$. Let $N_{\mathrm{Li}}(\mathbf{x}, t)$ denote the molar concentration of lithium atoms at a spatial point $\mathbf{x}$ in the particle at time t. Define the lithium occupancy as $\theta(\mathbf{x}, t) \equiv N_{\mathrm{Li}}/N_{\mathrm{L}}$ where N_{L} ($49194\ \mathrm{mol\ m^{-3}}$)[3] is the molar concentration of lithium sites within the NMC crystal. Write $\mathcal{F}(N_{\mathrm{Li}}, T)$ as the Helmholtz free-energy per unit volume of the NMC crystal at a temperature T. The chemical potential μ^c_{Li} (the superscript c denotes cathode) of the lithium atoms within the NMC crystal is then

$$\mu^c_{\mathrm{Li}}(\theta) = \left.\frac{\partial \mathcal{F}}{\partial N_{\mathrm{Li}}}\right|_T = \frac{1}{N_{\mathrm{L}}}\left.\frac{\partial \mathcal{F}}{\partial \theta}\right|_T. \qquad [2]$$

Charging/discharging is associated with the flux of lithium ions, but the crystal remains electrically neutral due to the counter flux of electrons from the current collector. The chemical potential $\mu^c_{\mathrm{Li}^+}$ of the lithium-ions in the electroneutral NMC crystal is

$$\mu^c_{\mathrm{Li}^+} = \left.\frac{\partial \mathcal{F}}{\partial N_{\mathrm{Li}^+}}\right|_T. \qquad [3]$$

To calculate $\mu^c_{\mathrm{Li^+}}$, recall that the addition of a neutral lithium atom is equivalent to addition of a lithium-ion and an electron such that

$$\mu^c_{\mathrm{Li}} \equiv \left.\frac{\partial \mathcal{F}}{\partial N_{\mathrm{Li}}}\right|_T = \left(\frac{\partial \mathcal{F}}{\partial N_{\mathrm{Li^+}}}\right)\left(\frac{\partial N_{\mathrm{Li^+}}}{\partial N_{\mathrm{Li}}}\right)\Big|_T + \left(\frac{\partial \mathcal{F}}{\partial N_{\mathrm{el^-}}}\right)\left(\frac{\partial N_{\mathrm{el^-}}}{\partial N_{\mathrm{Li}}}\right)\Big|_T, \quad [4]$$

where $N_{\mathrm{el^-}}$ denotes the molar concentration of electrons. Since the NMC remains electroneutral, the above differentiation is subject to the constraint $N_{\mathrm{Li^+}} = N_{\mathrm{Li}} = N_{\mathrm{el^-}}$. With the chemical potential of the electrons (often referred to as the Fermi level) defined as $\mu^c_{\mathrm{el^-}} \equiv \partial \mathcal{F}/\partial N_{\mathrm{el^-}}$, we have

$$\mu^c_{\mathrm{Li^+}} = \mu^c_{\mathrm{Li}} - \mu^c_{\mathrm{el^-}}\,. \quad [5]$$

The Fermi level $\mu^c_{\mathrm{el^-}}$ of the NMC particle is taken to be independent of θ and depends only on the electrical potential ϕ^c of the NMC crystal. Therefore, we set $\mu^c_{\mathrm{el^-}} = -F\phi^c$, where F is the Faraday constant. The chemical potential of the lithium-ions follows as

$$\mu^c_{\mathrm{Li^+}}(\theta) = \mu^c_{\mathrm{Li}}(\theta) + F\phi^c\,. \quad [6]$$

An expression for the chemical potential $\mu^c_{\mathrm{Li}}(\theta)$ is deduced from the open-circuit voltage versus occupancy profile as measured in the GITT experiment (see **Figure S1A**). The GITT experiment is performed on a cell having an NMC cathode with the Lithium metal anode. The chemical potential of the Lithium metal in the anode is given by a relation analogous to Equation 6 but with the reference chemical potential μ^a_{Li} now a constant since the occupancy of Li in the metal anode is fixed. We thus write the chemical potential of the Li ions in the anode as

$$\mu^a_{\mathrm{Li^+}} = \mu^a_{\mathrm{Li}} + F\phi^a\,, \quad [7]$$

where the superscript a denotes anode and ϕ^a is the electrical potential of the anode.

In the GITT experiments, open-circuit conditions for the cell are achieved by switching off the external current supply and allowing the cell to attain electrochemical equilibrium. In this state, the chemical potentials of the Li ions in the cathode and the anode are equal, i.e.

$$\mu^c_{\mathrm{Li^+}} = \mu^a_{\mathrm{Li^+}} \;\Rightarrow \mu^c_{\mathrm{Li}}(\theta) = -FV_{oc}(\theta) + \mu^a_{\mathrm{Li}}, \quad [8]$$

where $V_{oc}(\theta) \equiv \phi^c - \phi^a$ is the occupancy-dependent open-circuit voltage. Combining Equations 6 and 8 yields the chemical potential of $\mathrm{Li^+}$ ions in the cathode as

$$\mu^c_{\mathrm{Li^+}}(\theta) = -FV_{oc}(\theta) + \mu^a_{\mathrm{Li}} + F\phi^c\,. \quad [9]$$

The driving force **f** on the lithium-ions is obtained by the spatial gradient of chemical potential, i.e., $\mathbf{f} = -\boldsymbol{\nabla}\mu^{c}_{\mathrm{Li}^{+}}$. The drift velocity $\mathbf{v}_{\mathrm{drift}}$ is assumed to be proportional to the driving force and is given by $\mathbf{v}_{\mathrm{drift}} = -\mathbf{M}\cdot\boldsymbol{\nabla}\mu^{c}_{\mathrm{Li}^{+}}$ in terms of the mobility tensor **M** which is related to the diffusivity tensor **D** through the Einstein relation $\mathbf{M} = (1/RT)\mathbf{D}$. The layered structure of NMC allows lithium diffusion only within the basal plane with the diffusivity isotropic within the basal plane. Upon denoting the occupancy-dependent effective diffusivity within the basal plane by $D^{\mathrm{eff}}_{\mathrm{Li}}$, the transversely isotropic **D** in the crystallographic basis is given by

$$\mathbf{D} = \begin{bmatrix} D^{\mathrm{eff}}_{\mathrm{Li}} & 0 & 0 \\ 0 & D^{\mathrm{eff}}_{\mathrm{Li}} & 0 \\ 0 & 0 & 0 \end{bmatrix}, \qquad [10]$$

where $D^{\mathrm{eff}}_{\mathrm{Li}} \equiv D_{\mathrm{Li}}/S$. Here, D_{Li} is the diffusion co-efficient obtained from the occupancy-dependent hop rate ν of Li^{+} ions in the NMC lattice as obtained by the NMR experiments (see Supplementary Section 2, below) and S is a scaling co-efficient that is calibrated using a procedure described below. Assuming isotropic diffusion in the two dimensional (2D) basal plane it follows that

$$D_{\mathrm{Li}} = \nu\langle r^2\rangle/4\,, \qquad [11]$$

where $\langle r^2\rangle$ is the mean-square distance the Li^{+} ion travels per hop. Assuming Li^{+} ions hop between adjacent, octahedral lattice sites, we expect $\langle r^2\rangle$ to scale with a representative lattice parameter and thus we set $\langle r^2\rangle = l^2$ where l is the lattice parameter in the ab-plane. The NMR-derived hopping rate gives a discrete set of diffusivity data shown in **Figure S1B**. We fit a smooth curve through the measured data points using piecewise cubic interpolation functions with the diffusivity assumed to be constant at the two extremes in the occupancy: for $0 \le 1-\theta \le 0.07$ and $0.9 \le 1-\theta \le 1$ we assume D_{Li} to be independent of θ and possess the values 0.016×10^{-11} cm^2/s [5]and 0.059×10^{-11} cm^2/s, respectively.

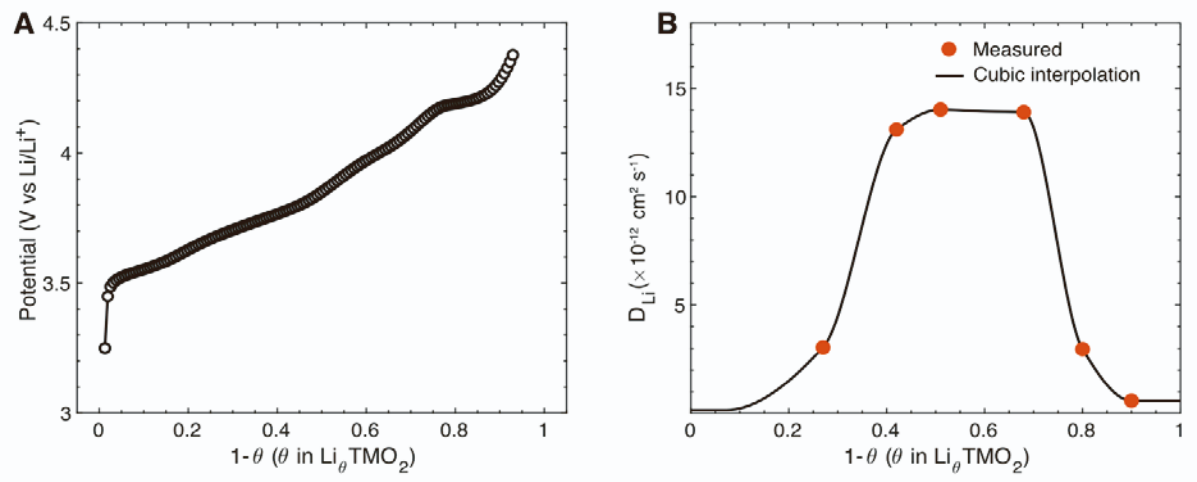

Figure S1. Open circuit voltage and Li^+ hop rate. (**A**) Open circuit voltage (V_{oc}) measured at different states of charge in the GITT experiment. (**B**) The **ab-** plane diffusivity obtained from the Li^+ hop rate. The NMR data is shown as discrete data points and a smooth curve using piecewise cubic interpolation functions is fitted to this data for use in the numerical simulations.

The flux of Li^+ ions follows from Equation 9 as

$$\mathbf{J} = N_{\mathrm{Li}^+}\mathbf{v}_{drift} = -\frac{N_{\mathrm{L}}}{RT}\theta\mathbf{D}\cdot\boldsymbol{\nabla}\mu^{c}_{\mathrm{Li}^+} = \frac{N_{\mathrm{L}}F}{RT}\theta\mathbf{D}\cdot\frac{\partial V_{oc}}{\partial\theta}\boldsymbol{\nabla}\theta, \qquad [12]$$

where we have used the fact that the electrical potential within the NMC particle is spatially uniform (it is a good electron conductor) and hence the spatial gradient of ϕ^c vanishes. The formulation is completed via the conservation law

$$\frac{\partial N_{\mathrm{Li}^+}}{\partial t} = -\boldsymbol{\nabla}\cdot\mathbf{J}, \qquad [13]$$

which can then be solved with appropriate initial and boundary conditions, as follows.

Boundary value problem and initial conditions. With a vanishing flux along the $\boldsymbol{c}$ axis the problem reduces to a two-dimensional (2D) problem in the basal plane. The shape and size of the particle in the $\boldsymbol{ab}$ −plane is obtained from the optical and SEM images (Figures 1B and 1C). Let Ω denote the domain of the NMC particle, and the boundary with the electrolyte (reactive surface) is denoted by $\partial\Omega$ (**Figure S2A**). The governing equation (Equation 13) for the 2D problem in the basal plane reduces to

$$N_{\mathrm{L}}\frac{\partial\theta}{\partial t} = -\left[\frac{\partial}{\partial x_1}\left(\frac{N_{\mathrm{L}}F}{RT}\theta D^{\mathrm{eff}}_{\mathrm{Li}}\frac{\partial V_{oc}}{\partial\theta}\frac{\partial\theta}{\partial x_1}\right) + \frac{\partial}{\partial x_2}\left(\frac{N_{\mathrm{L}}F}{RT}\theta D^{\mathrm{eff}}_{\mathrm{Li}}\frac{\partial V_{oc}}{\partial\theta}\frac{\partial\theta}{\partial x_2}\right)\right], \qquad [14]$$

with initial conditions $\theta = \theta_0\ \forall \mathbf{x} \in \Omega$ and boundary conditions $\mathbf{J} \cdot \mathbf{n} = j$ for $t \geq 0$ on $\partial\Omega$. At the beginning of the delithiation process, the particle has an occupancy of $\theta_0 = 0.95$ while the imposed surface flux j was used to match the experimental conditions as follows. Galvanostatic experiments were performed for a given C-rate (denoted as nC), which must be related to the boundary flux j. Let Q_{NMC} and ρ_{NMC} denote the nominal capacity of NMC and density of active material. Recalling that the prismatic NMC particle with no diffusion in the $\boldsymbol{c}$ −direction reduces to a 2D problem in the $\boldsymbol{ab}$ −plane, the NMC particle geometry is defined by its cross-sectional area A_{ab} and perimeter Γ_{ab} in the $\boldsymbol{ab}$ −plane. Then, for a charging rate of nC, the flux j is given by

$$j = n\, Q_{NMC}\, \rho_{NMC}\, \frac{A_{ab}}{\Gamma_{ab}}. \qquad [15]$$

In all calculations presented we have assumed[6] $Q_{NMC} = 210\ \mathrm{mA\,h\,g^{-1}}$ and $\rho_{NMC} = 4.78\ \mathrm{g\,cm^{-3}}$, while the standard particle geometry (Figure 3A) has $A_{ab} = 4.87\ \mu\mathrm{m}^2$ and $\Gamma_{ab} = 8.06\ \mu\mathrm{m}$. The governing Equation 14 was solved via the finite-element method using COMSOL Multiphysics®. The outputs from the simulations are the lithium occupancies in the particle as a function of spatial coordinates (x_1, x_2) and time t. Lithiation calculations were conducted in a similar manner, assuming an initial occupancy of $\theta_0 = 0.2$ and assuming that the fully lithiated state has an occupancy of $\theta = 0.95$.

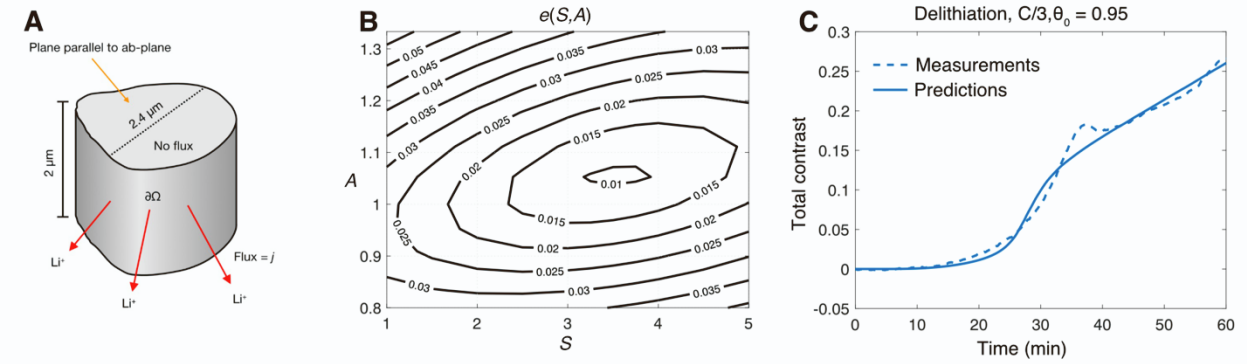

Figure S2. Calibration of the scaling factor. (A) Schematic of the NMC particle used in the simulation. (**B**) Contour plot of the error function $e(S, A)$ for the C/3 delithiation experiment. The global minimum of error is attained at $(S, A) = (3.5, 1/0.95)$. (**C**) Comparison between measurements and predictions of the total contrast at the center of the particle in the C/3 delithiation experiment with $(S, A) = (3.5, 1/0.95)$.

Calibration of the scaling factor *S*

To make a quantitative comparison between the experiments and simulation predictions, we calibrate the model using the total contrast data at the particle center in a C/3 delithiation

experiment. A linear relation between total contrast (defined in Equation 1) and occupancy is assumed such that

$$\frac{I - I_0}{I_0} = A(1 - \theta) + B, \qquad [16]$$

where A and B are unknown constants. The assumption that the particle delithiates from an initial occupancy of $\theta_0 = 0.95$ (i.e., $I = I_0$ at $\theta = \theta_0 = 0.95$) implies that $B = -A(1 - \theta_0)$ and Equation 16 reduces to

$$\bar{I}(t) \equiv \left[\frac{I(t)}{I_0} - 1\right] = A[\theta_0 - \theta(t)]. \qquad [17]$$

This allows for an estimation of the total contrast $\bar{I}(t)$ at time t from the prediction of the occupancy $\theta(t)$ at the same time t if the constants (S, A) are known. These constants are calibrated by comparing measurements and predictions of the total contrast in a C/3 delithiation experiment as follows.

Let $\bar{I}_k^{\text{measured}}$ denote the total contrast at the particle center at $'k^{\text{th}}'$ time point measured during the C/3 delithiation experiment. Using our finite element simulations, we extract the occupancy θ_k at the particle centre for C/3 delithiation at precisely the same time point. We define a root-mean-square error $e(S, A)$ to quantify the difference between the measurements and model predictions as

$$e(S, A) \equiv \sqrt{\frac{1}{M}\sum_{k=1}^{M}\left[\bar{I}_k^{\text{measured}} - A(\theta_0 - \theta_k)\right]^2}, \qquad [18]$$

where M denotes the total number of time points in the C/3 delithiation experiment. The constants (S, A) are then determined by minimizing $e(S, A)$. A contour plot of $e(S, A)$ is shown in **Figure S2B** where it is evident that a unique global minimum is attained at $S = 3.5$ and $A = 1/0.95$. The corresponding comparison between the measured and predicted $\bar{I}(t)$ at the centre of the particle in the C/3 delithiation is shown in **Figure S2C** using $(S, A) = (3.5, 1/0.95)$. The excellent agreement confirms the quality of the calibration. The fidelity of the model is then evaluated by comparing spatio-temporal measurements and predictions in the C/3 delithiation experiment (**Figure 3E**): again good agreement is obtained.

Supplementary Section 2: ssNMR and self-diffusion coefficients

The application of ^{7}Li NMR to study LIB positive electrode materials is a robust method for probing local Li environments, with great sensitivity to surrounding paramagnetic TM ions.[7] Whereas ^{7}Li in a range of diamagnetic environments resonates very close to the Li_2CO_3 reference compound (*i.e.*, near 0 ppm), hyperfine interactions with unpaired electrons can induce shifts of > 100 ppm. This can allow for considerable insight into the local chemical environment of Li atoms, even when there are many different sites within the same material.

Figure S3 shows MATPASS spectra of $Li_{\theta}Ni_{0.87}Mn_{0.05}Co_{0.08}O_2$ at various SOC. The advantage of the MATPASS methodology is that it allows the isotropic resonances to be observed without overlap from the spinning sidebands of other resonances; this is particularly important in this system which contains multiple environments and hence considerable overlap between the isotropic resonances and sidebands are seen in single pulse MAS NMR spectrum when typical magnetic field strengths and MAS frequencies are used. The MATPASS spectra show broad signals, which are consistent with the expected broadening from the high amount of paramagnetic species in the sample and the very large number of local chemical environments, each of which contributes a unique ^{7}Li hyperfine shift.

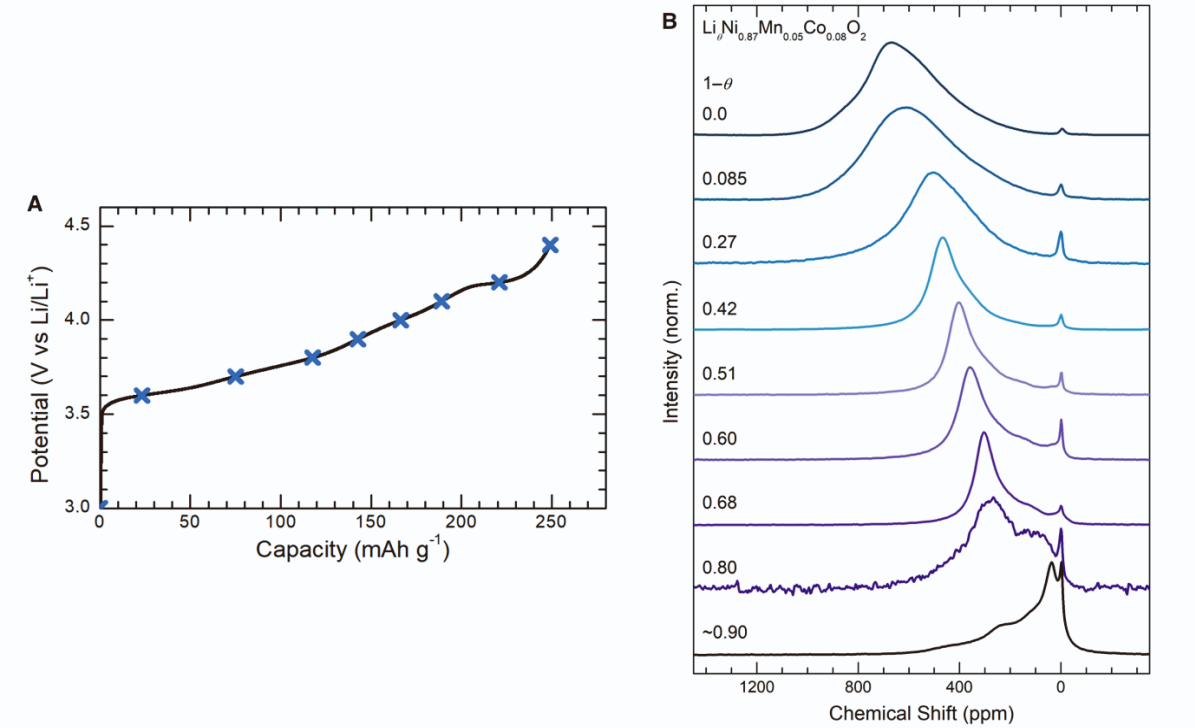

Figure S3. ssNMR results of the NMC cathode at various SOCs. ^{7}Li MATPASS spectra measured from $Li_{\theta}Ni_{0.87}Mn_{0.05}Co_{0.08}O_2$ at various values of $1–\theta$, as indicated on the figure. Intensities are normalised to the most intense peak. MAS, 60 kHz.

As the NMC material is delithiated (*i.e.*, charged), the peak position moves to lower chemical shift. This is consistent with the expected behaviour for NMC materials; as Li is removed, Ni^{2+} and Ni^{3+} ions are oxidised to Ni^{4+}. Since Ni^{4+} is diamagnetic, a decrease in the average chemical shift of the ^{7}Li signal occurs. To provide further insights, the ^{7}Li MATPASS NMR spectra were modelled using the random solution model of Märker *et al.*,[3] which is based on previously published methods.[8,9] To a very good approximation, the hyperfine interaction with nearest neighbours is additive – *i.e.*, the influence of the various adjacent TMs on the ^{7}Li chemical shift can be predicted through a simple summation. The full methodology of chemical shift and line-width prediction is the same as described in Ref[3]. This model incorporates Li hopping between lattice sites using the formula derived by Norris.[10]

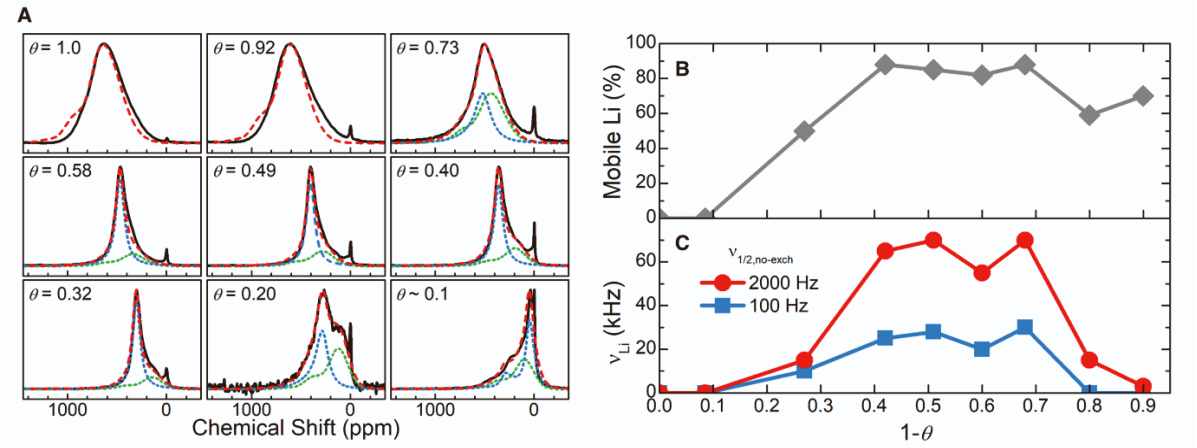

Figure S4. Modelling of ^{7}Li MATPASS spectra of $Li_\theta Ni_{0.87}Mn_{0.05}Co_{0.08}O_2$. (A) Each panel shows the experimental spectrum (black, identical to Figure S3B) together with the calculated spectrum (dashed red). The calculated spectra for θ = 1.0 and 0.92 were obtained using the model with only immobile Li (*i.e.*, without Li hopping). The other spectra are the calculated sum (dashed red) of the mobile (dotted blue) and immobile (dotted green) Li ions. The peak at ~0 ppm arises from diamagnetic lithium salts (*e.g.*, Li_2CO_3) and is not included in the model. (B) Percentage of the ^{7}Li attributed to 'mobile' Li that hops between local sites (for $\nu_{1/2,no\text{-}exch}$ = 2 kHz). (C) Hopping frequency (ν_{Li}) of the mobile Li. Two values for $\nu_{1/2,no\text{-}exch}$ were used for the calculation of spectra to estimate the maximum (red, circles) and minimum (blue, squares) values of ν_{Li}. For spectra where there was no observable mobile Li, the frequency is presented as zero.

At low SOC ($\theta \rightarrow 1$), the spectra can be reproduced by assuming all Li is 'immobile', *i.e.*, any hopping between adjacent sites is negligible on the timescale of the NMR measurement (Figure 3). The peak shape is not a perfect fit with the random solution model, suggesting there may be some preferential, partial TM ordering, such as the occurrence of Ni^{2+}–Mn^{4+} pairs or of larger TM clusters, as described previously for other NMC stoichiometries.[11,12] This is consistent with the findings of Märker for NMC811, although this effect appears less pronounced in the $LiNi_{0.87}Mn_{0.05}Co_{0.08}O_2$ sample used here. Future studies will further investigate the relationship between Ni-content and local TM ordering in Ni-rich NMC materials.

At intermediate SOC, modelling the spectra requires introducing 'mobile' Li, where the Li ions rapidly hop between different local sites. This results in sharper peak shapes that average the chemical shifts of several local chemical environments. The value of this hopping frequency (ν_{Li}) directly affects the peak width. The value of this measurement for the present work is that the model introduces a hopping frequency, which is related to the self-diffusivity of Li in the electrode material. In practice, the evaluation of ν_{Li} requires knowledge of the peak width in the absence of site exchange, $\nu_{1/2,no\text{-}exch}$. This value is affected by the ^{7}Li spin-spin relaxation times, by inhomogeneous broadening caused by distributions in the local environment and other sources of broadening not removed by MAS including anisotropic bulk magnetic susceptibility effects. Whereas the peak widths are not exactly known, it was shown estimated that it lies in the range 100 Hz $\leq \nu_{1/2,no\text{-}exch} \leq$ 2 kHz. [3] Therefore, ν_{Li} was here evaluated at these two limits to estimate the minimum and maximum values (Figure S4C). In general, the NMR linewidths are inversely related to the transverse relaxation constant T_2. Whereas these values are unknown for the samples in this work, it is generally true that relaxation in the transverse plane is at least as fast as relaxation in the longitudinal direction, *i.e.*, $T_1 \geq T_2$. On the basis of the measured T_1 times, the minimum linewidths were evaluated according to Equation 19 (Table S1):

$$\nu_{1/2} \geq (\pi T_1)^{-1} \qquad [19]$$

The values are consistent with the range used to model the spectra.

Table S1. ^{7}Li MAS-NMR T_1 relaxation times were measured as a function of x in $Li_xNi_{0.87}Mn_{0.05}Co_{0.08}O_2$ by saturation-recovery. T_1 times are for the bulk NMC signal (but not for the signals of diamagnetic Li salts at ~0 ppm). Minimum linewidths as evaluated using Equation 19 are shown.

$1-\theta$	T_1 (ms)	$\nu_{1/2,min}$ (Hz)
0.0	4.61	69.0
0.085	5.38	59.2
0.27	5.82	54.7
0.42	6.39	49.8
0.51	7.54	42.2
0.60	8.25	38.6
0.68	8.51	37.4
0.80	4.82	66.0
~0.9	5.60	56.8

The diffusion coefficients used in the finite element simulations used the fastest hop rates obtained by assuming that the linewidth of the resonances is 2kHz. A scaling factor of 3.5 was needed to reconcile the experimental and modelling data. This difference is ascribed to: (i) The choice of the highest estimates for the hopping frequency; the lower values are approximately 2.5 times lower. (ii) Not all the Li^+ ions are mobile; a subset remain rigid, within the NMR timescale indicating that there is a distribution of correlations times, (iii) We set the root-mean-square hop distance $\sqrt{\langle r^2 \rangle}$

equal to the ab-plane lattice parameter l in Equation 11 by assuming Li^+ ions only hop between adjacent octahedral lattice sites. (iv) Finally, the hop rates are that of the bulk, and one aim is to determine whether D varies from particle to particle. If we instead use the lowest hop rates derived in the NMR simulations and scale the hop rates according to the fraction of mobile ions in the triangular lattice a scaling factor similar to that obtained in the simulations is obtained. This may be fortuitous, since a full analysis would require for example, treating 'immobile' Li^+ ions as diffusion obstacles[13] (for an example discussion of anomalous tracer diffusion in the presence of obstacles on a triangular lattice, see Lončarević et al.). Furthermore, the present model also assumes Li^+ ions behave as an ideal lattice gas, i.e., that their hopping frequency is not affected by the number of nearest neighbours and they do not hop in pairs or clusters. However, exploring more detailed models and connecting them with the NMR data is beyond the scope of the present work.

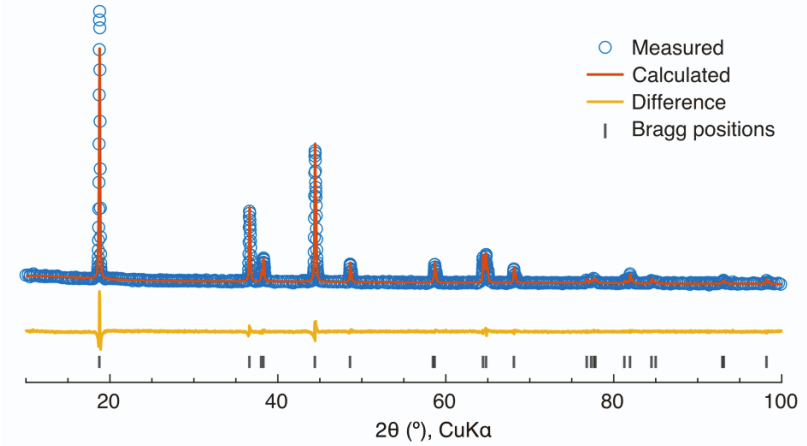

Figure S5. X-ray diffraction pattern and Rietveld refinement results. Lattice constants: a = 2.87551(7) Å, c = 14.1944(5) Å; unit cell volume: 101.643(6) Å^3. Li/Ni paired antisite defects: 2.0%. Fitting quality: R_{wp} = 3.43%, R_{exp} = 1.50%, gof = 2.28.

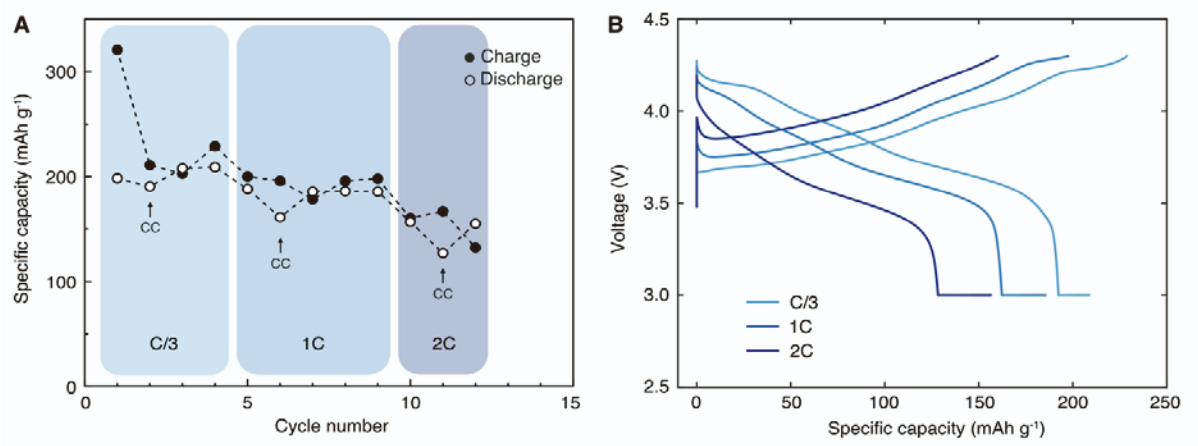

Figure S6. Electrochemistry of the single-crystal NMC in the optical cell. (**A**) Capacity retention. (**B**) representative voltage profile at C/3, 1C and 2C.

The electrochemical performance of the optical cell is summarised in **Figure S6**. Briefly, reversible capacities of ~200, 185 and 155 mAh g^{-1} are achieved at C/3, 1C and 2C, respectively under CC-CCCV condition (constant-current charge and constant-current constant-voltage discharge; 2 hours voltage hold at 3 V). These values are lower than what was achieved with the same self-standing electrodes in coin cells (225, 210, 190 mAh g^{-1} at C/3, 1C and 2C, respectively; **Figure S7**), which is likely due to the limited performance of the specialised optical cell as compared to standard coin cells as evidenced by the higher voltage hysteresis. It is worth noting that the optical cell generally exhibits lower coulombic efficiencies during the initial cycles. More precisely, the charge capacity obtained is noticeably higher than expected, while the discharge

capacity is reasonably representative of the typical behaviour of the material. We attribute this to (1) irreversible oxidative side reactions occurring in the optical cell during the charging process (2) high proportions of carbon black in the self-standing electrodes (see **Figure S7**).

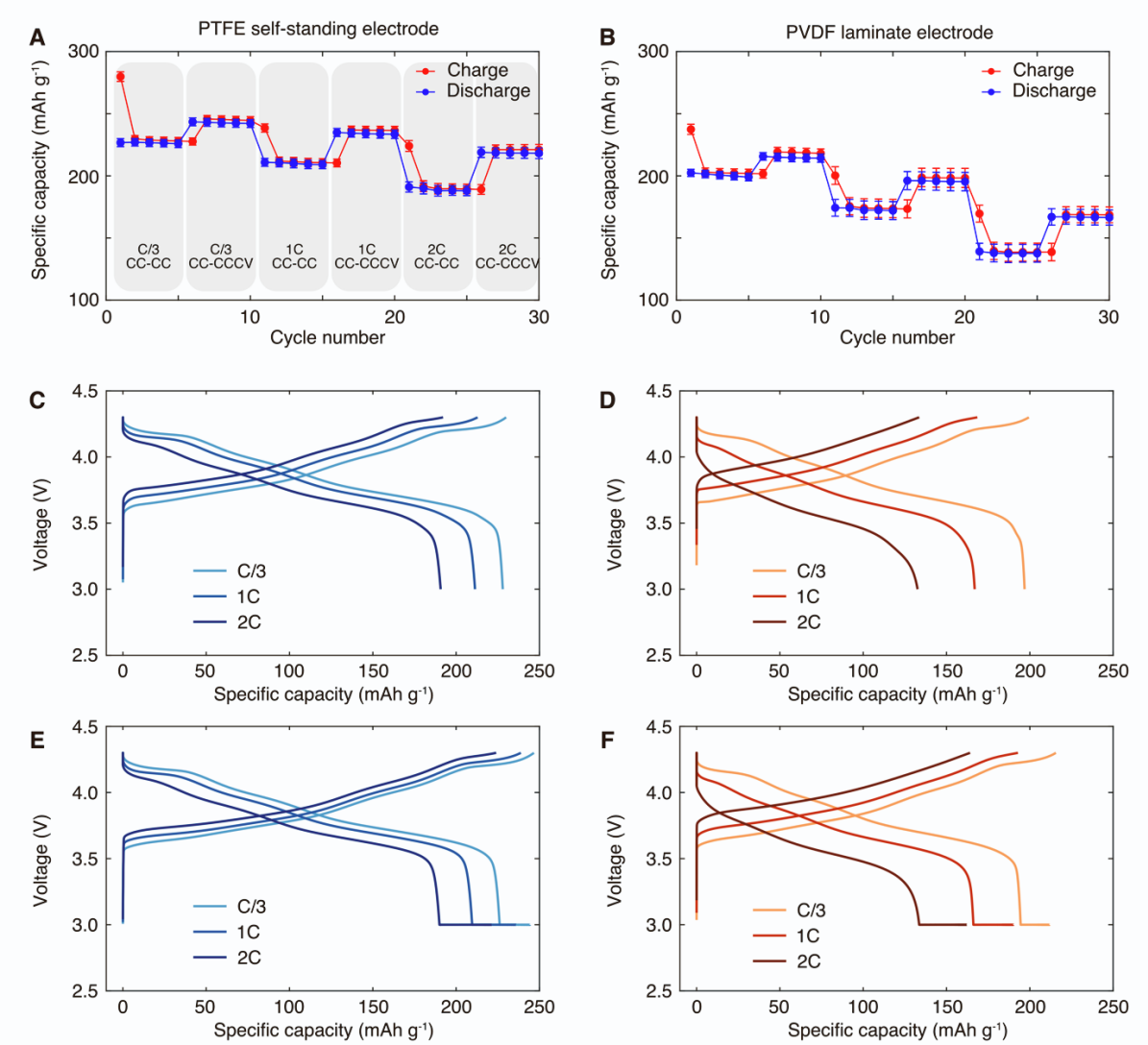

Figure S7. Electrochemistry of the single-crystal NMC material at various C-rates in coin cells. (**A, C, E**) Self-standing electrodes: (**A**) Capacity retention at C/3, 1C and 2C under CC-CC and CC-CCCV charge-discharge cycles, (**C**) Voltage profiles of CC-CC cycles, (**E**) Voltage profiles of CC-CCCV cycles. (**B, D, F**) Laminate electrodes: (**B**) Capacity retention at C/3, 1C and 2C under CC-CC and CC-CCCV charge-discharge cycles, (**D**) Voltage profiles of CC-CC cycles, (**F**) Voltage profiles of CC-CCCV cycles.

Note a higher carbon content results in a higher first-cycle irreversible coulombic loss. This is shown by the fact that the PTFE self-standing electrodes exhibits ~280 mAh g^{-1} on the first charge, which is higher than the theoretical capacity of the NMC material (275 mA h g^{-1}). Error bars represent standard deviations of two parallel cells.

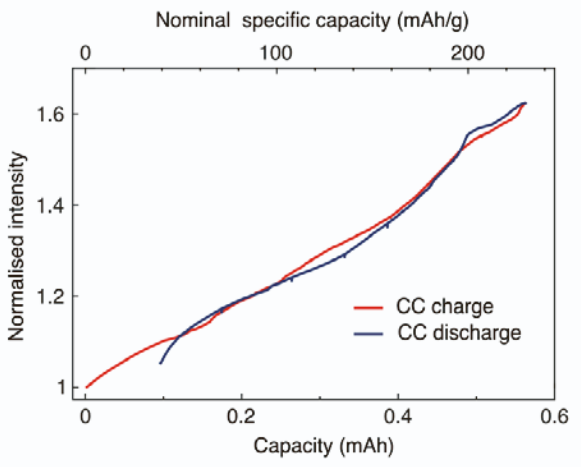

Figure S8. Normalised intensity change as a function of capacity during a C/3 CC-CC charge-discharge cycle. The nominal specific capacity is normalised to the mass of the NMC active material.

The difficulties in establishing a quantitative relationship between the optical intensity and the lithium content arise partly from the inaccurate determination of the true lithium content, caused by irreversible capacity contributions from side reactions as discussed above. These additional capacity contributions mean that the intensity-capacity profiles for the charge and discharge steps do not overlap, particularly at the low SoC region.

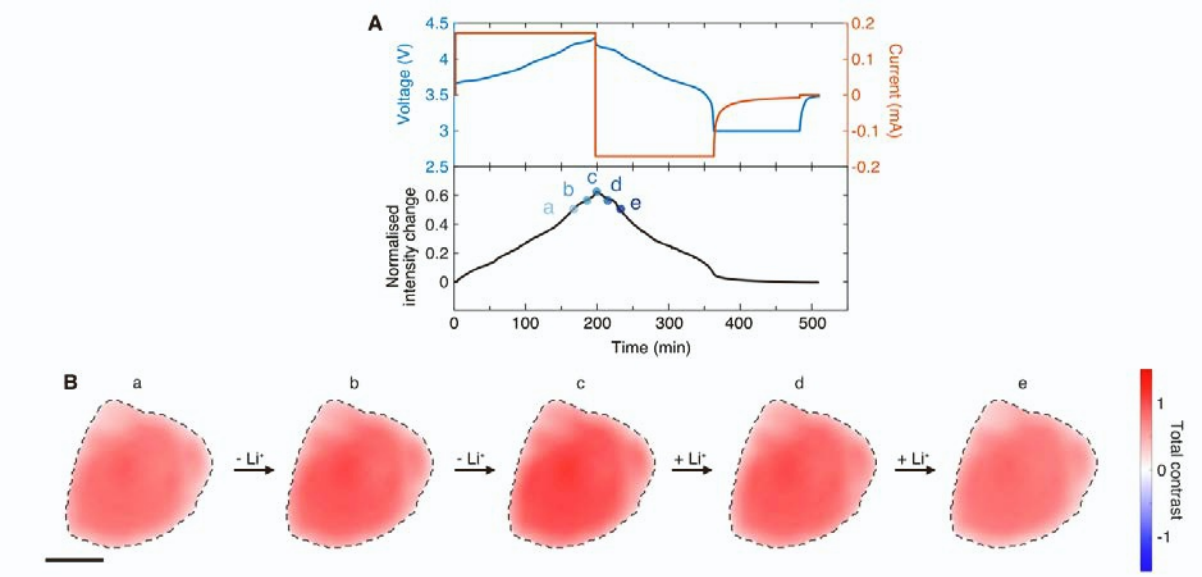

Figure S9. High voltage region. (**A**) Voltage and current profile (top panel) and normalised intensity during a C/3 rate CC charge and CCCV discharge cycle. Here, a, b, c, d, e and f are at 164.7, 184.7, 197.3, 218 and 231.3 min, respectively. (**B**) Differential images of an NMC active particle during the high voltage region. Scale bars, 1 μm.

High voltage plateau region. Intriguingly, the normalised optical intensity appears to follow a similar profile as the voltage (**Figure 1E**); in particular, the rate of change in intensity decreases when the cell voltage reaches the flatter region at around 4.2 V. For unsubstituted $LiNiO_2$, this region corresponds to a true voltage plateau which is associated with a first-order phase transition, known as the H2-H3 transition (where H denotes the hexagonal structure and the numbers the order in which each phase of that symmetry is observed on charge).[14,15] The origin of the phase transition in $LiNiO_2$ between two phases with the same symmetry ($R\bar{3}m$) is unclear, but in part may be due to the substantially smaller *c* lattice constant of the H3 phase. This transition disappears upon substitution of the transition metal (Ni) layers (for example, for NMCs and NCAs with 80% Ni, i.e., 20% substitution, no first-order H2-H3 transition is observed) even though a relatively flat voltage region is still visible (although less flat than that of $LiNiO_2$).[3,16,17] The optical results presented here indicate that the change in the dielectric properties of the NMC during this voltage window around 4.2 V may be different in behaviour to that in the lower voltage region, perhaps indicating that the 4.2 V process in NCA/NMCs has an electronic component to the mechanism. Moreover, the differential image analysis results show that the intensity changed uniformly across the particle during this high voltage window (i.e., no moving phase front was seen such as has previously been observed clearly for $LiCoO_2$),[1] confirming that no first-order H2-H3 transition occurs for the Ni-rich NMC particles studied here. Nevertheless, our results show that the structural and electronic properties of this group of materials are highly complex, and further studies are needed to advance the understanding of the underlying mechanisms.

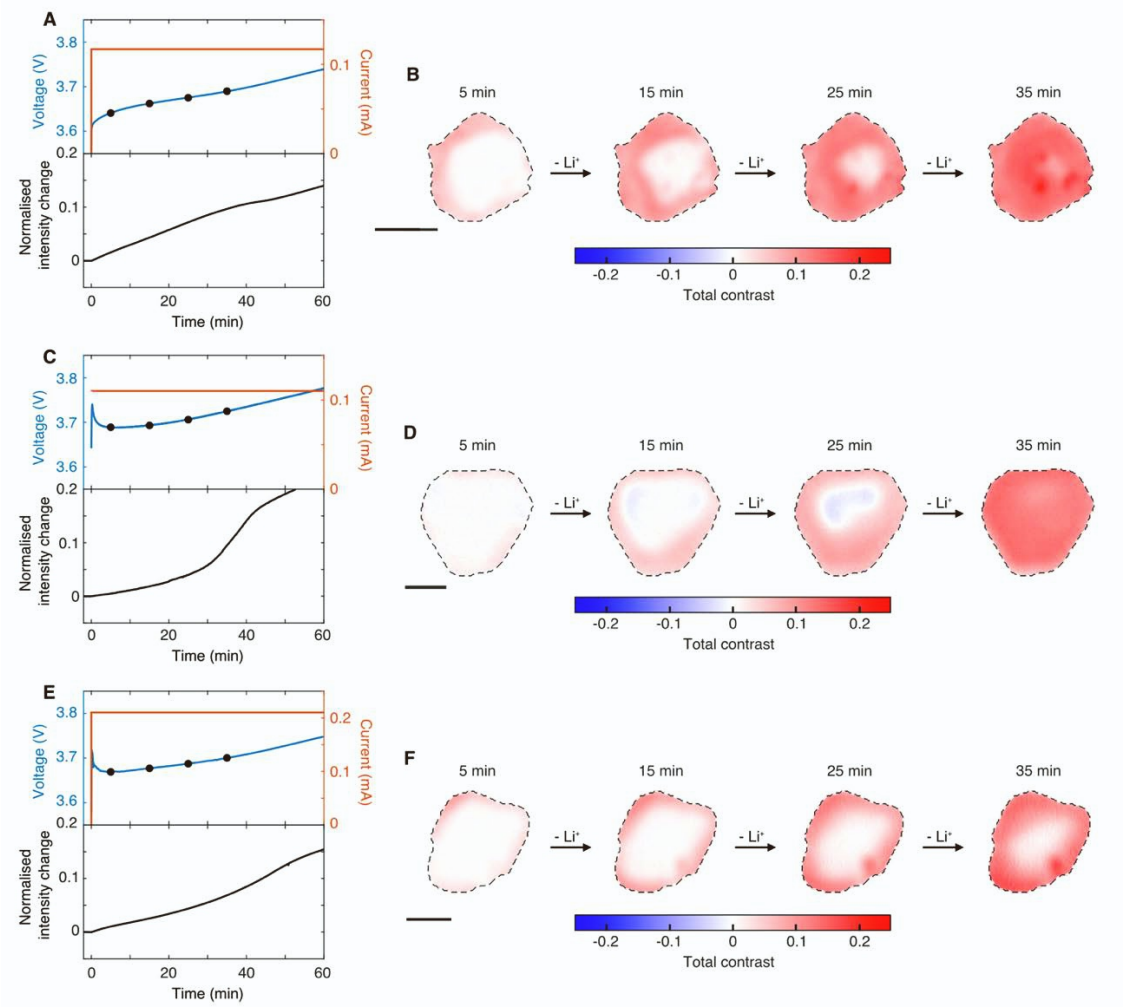

Figure S10. Reproducibility of the lithium heterogeneity at the beginning of charge. Three different particles, from different electrodes and in different cells, are shown here. (**A, C, E**) Voltage, current and normalised intensity change at a rate of C/3. (**B, D, F**) Corresponding differential images at the times indicated by black circles. Scale bars, 1 µm.

Note that a noticeable overpotential is observed at the beginning of charge, for instance in Figures 2C, S10C and S10E, while it is not visible for some others (Figures 1E, 2A, S10A). The presence of Li_2CO_3 on the surface of NMC particles is known to resulting in a voltage spike due to reaction heterogeneity at the intra-particle level.[16] However, such a spike typically exists only on the first charge, during which the Li_2CO_3 layer is decomposed. The charge and discharge profiles shown in Figures 2C, S6 and S10) are, however, subsequent cycles after initial pre-cycling conditions. Instead, we attribute the voltage bumps in Figures 2C, S6 and S10 to overpotentials originating from the unconventional geometry of the optical cell setup, which does not have metal foil current collectors to provide uniform electrical contact. This is supported by cycling the same PTFE electrodes in coin cells (rather than the optical cell), where they do not show such voltage bumps, as shown in Figure S7.

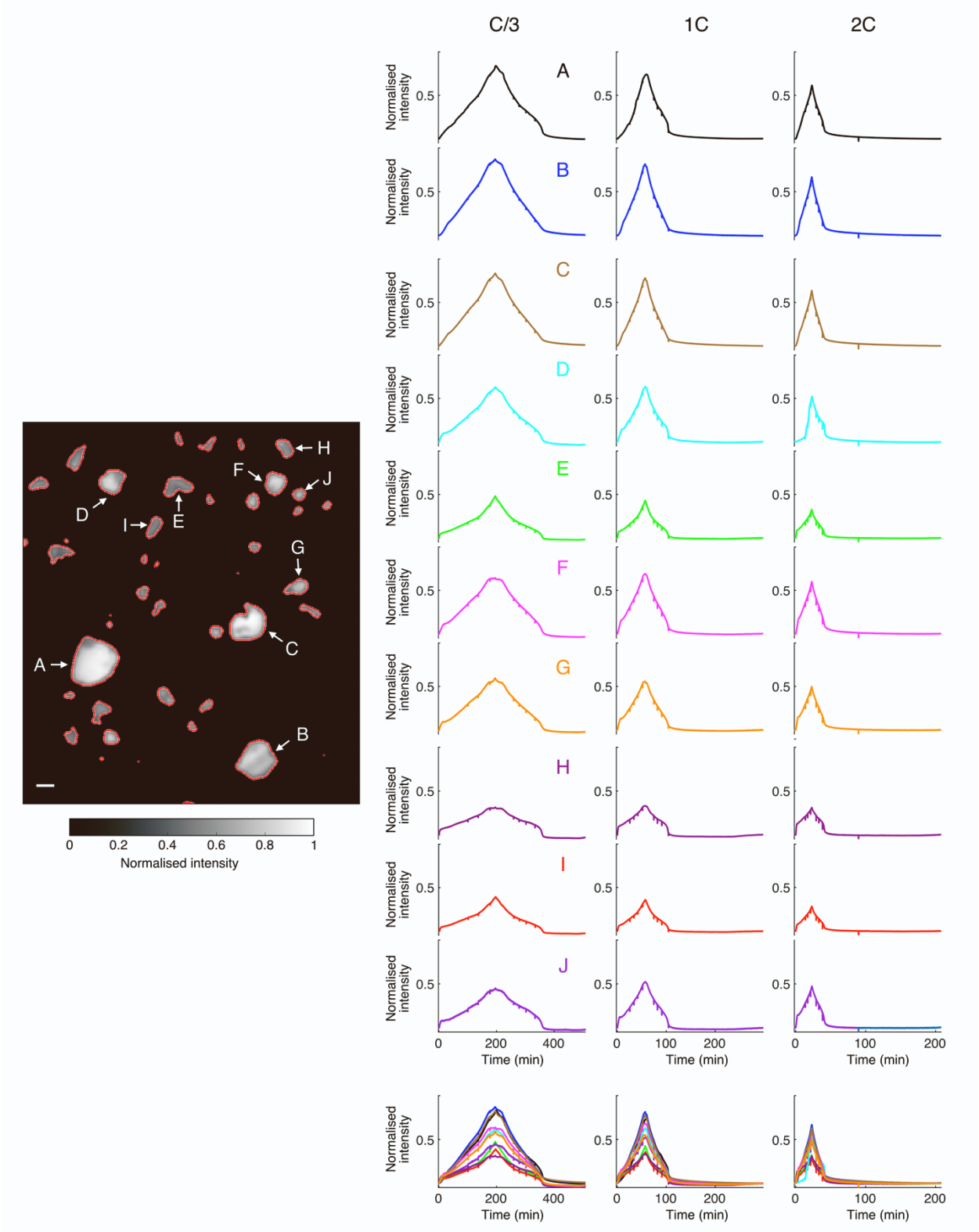

Figure S11. Inter-particle heterogeneity. Normalised intensity changes for multiple particles within the same electrode at various rates (C/3, 1C and 2C).

Inter-particle heterogeneity. All particles shown in **Figure S11** exhibited the general trend that the intensity increased on charge and decreased on discharge. In addition, the maximum normalised intensity (achieved at the end of charge) decreased as the rate increased from C/3 to 2C. Interestingly, the intensity increase for particle D was noticeably slower at the beginning of charge as compared to the others at 2C rate. Note that intensity values are not directly comparable between different particles because a number of factors contribute to the intensity values, for instance, particle size, observed facet, surface roughness, etc.

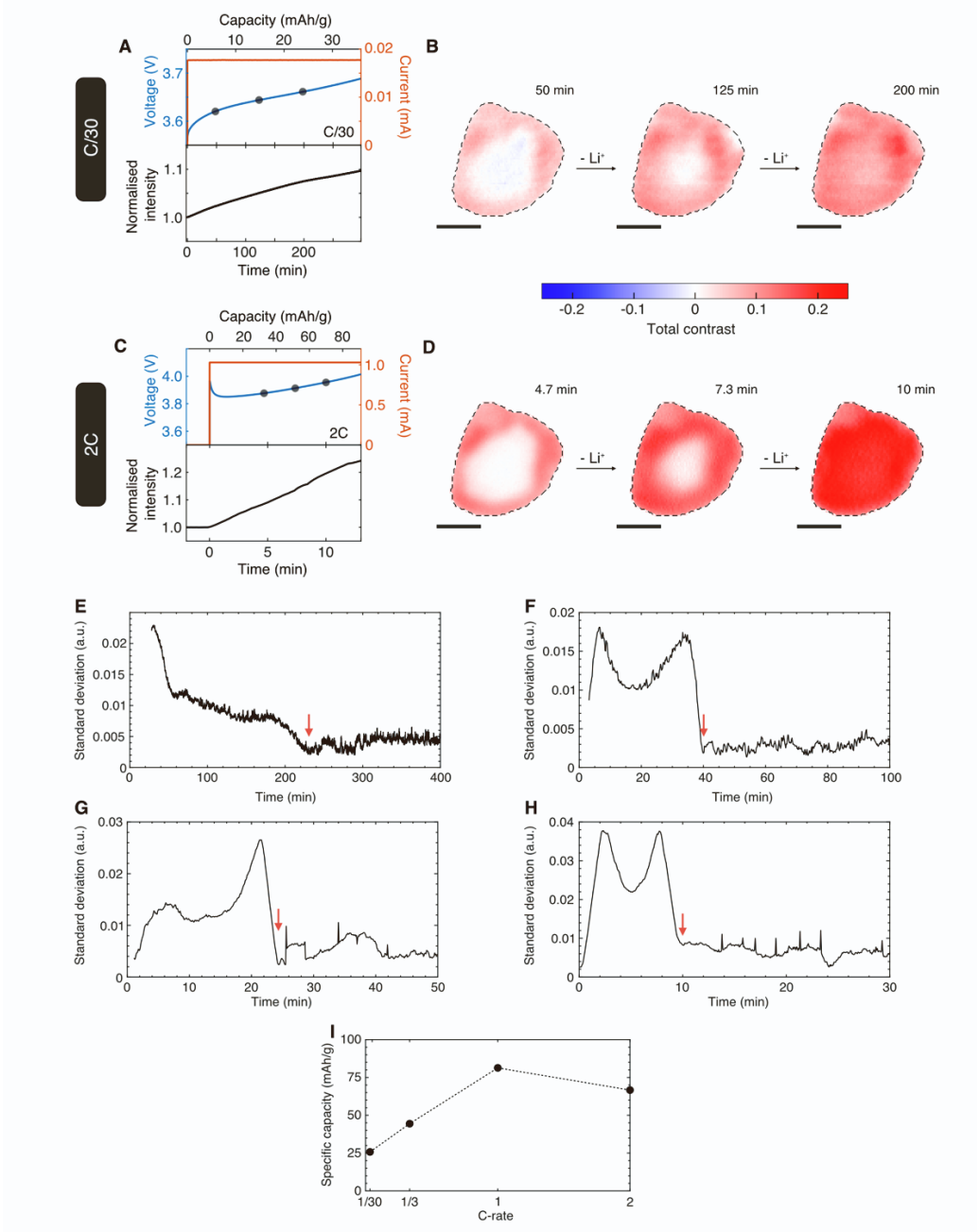

Figure S12. Rate response. (**A, B**) Voltage, current and normalised intensity change (A) and the representative differential images (B) at a rate of C/30. (**C, D**) Voltage, current and normalised intensity change (C) and the representative differential images (D) at a rate of 2C. (**E-H**) The evolution of the standard deviation of the 'sequential differential contrast' over the imaged particle pixels for C/30 (E), C/3 (F), 1C (G) and 2C (H). 'Sequential differential contrast' = $(I_k - I_{(k-x)})/I_{(k-x)}$, where I_k is the intensity of the k^{th} frame and $I_{(k-x)}$ is the intensity of the $(k-x)^{th}$ frame, which represents intensity changes occurring in the time interval between the pair of frames (x, 20 for C/30, 30 for C/3, 1C and 2C. Note for the C/30 dataset, every 20 frames were binned to improve statistics). Red arrows indicate a sharp drop in standard deviation which occurs when the

propagating delithiation front reaches the centre of the particle, marking the disappearance of the core-shell type lithium heterogeneity. (**I**) Summary of the specific capacities for the SoC range (based on cell electrochemistry, averaged over the entire electrode) where lithium heterogeneity is presented at various rates (C/30, C/3, 1C and 2C). The SoC range during which the heterogeneity exists widens as the rate increases from C/30 to 1C, but narrows slightly on further increase to 2C based on the optical results for this specific particle.

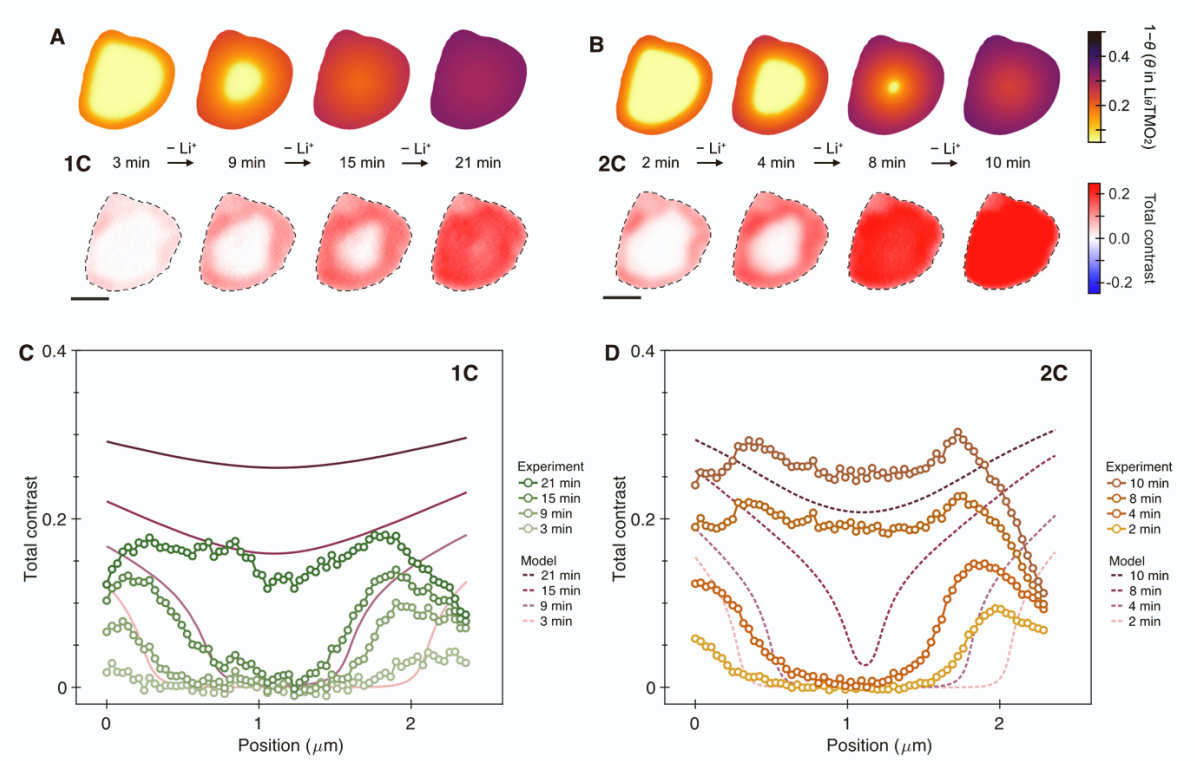

Figure S13. Comparing modelling and experimental results for the beginning of delithiation at various rates. Modelling and experimental results of delithiation 1C (**A, C**) and 2C rates (**B, D**), where the model used $D_{\mathrm{Li}}^{\mathrm{eff}} \equiv D_{\mathrm{Li}}/3.5$.

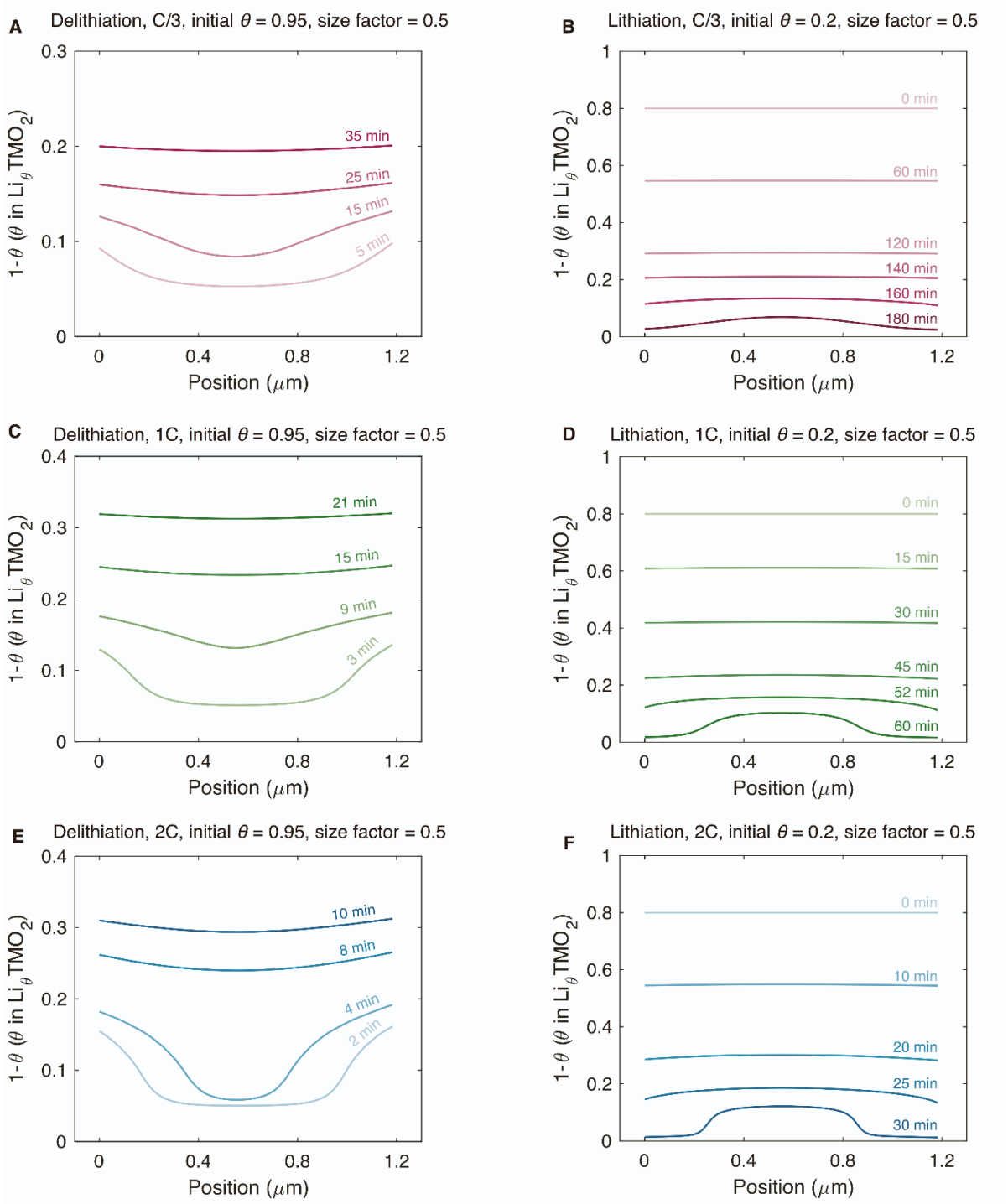

Figure S14. Effect of particle size on the lithium heterogeneity (size factor, 0.5). Modelling results showing the spatio-temporal variation of the degree of delithiation at: (**A**) C/3, (**C**) 1C, (**E**) 2C; and lithiation process: (**B**) C/3, (**D**) 1C, (**F**) 2C for a particle size of 1.2 μm and $D_{\mathrm{Li}}^{\mathrm{eff}} = D_{\mathrm{Li}}/3.5$. Lithium heterogeneity is significantly reduced at low C-rate of C/3 when compared to the original particle **Figure 3D**.

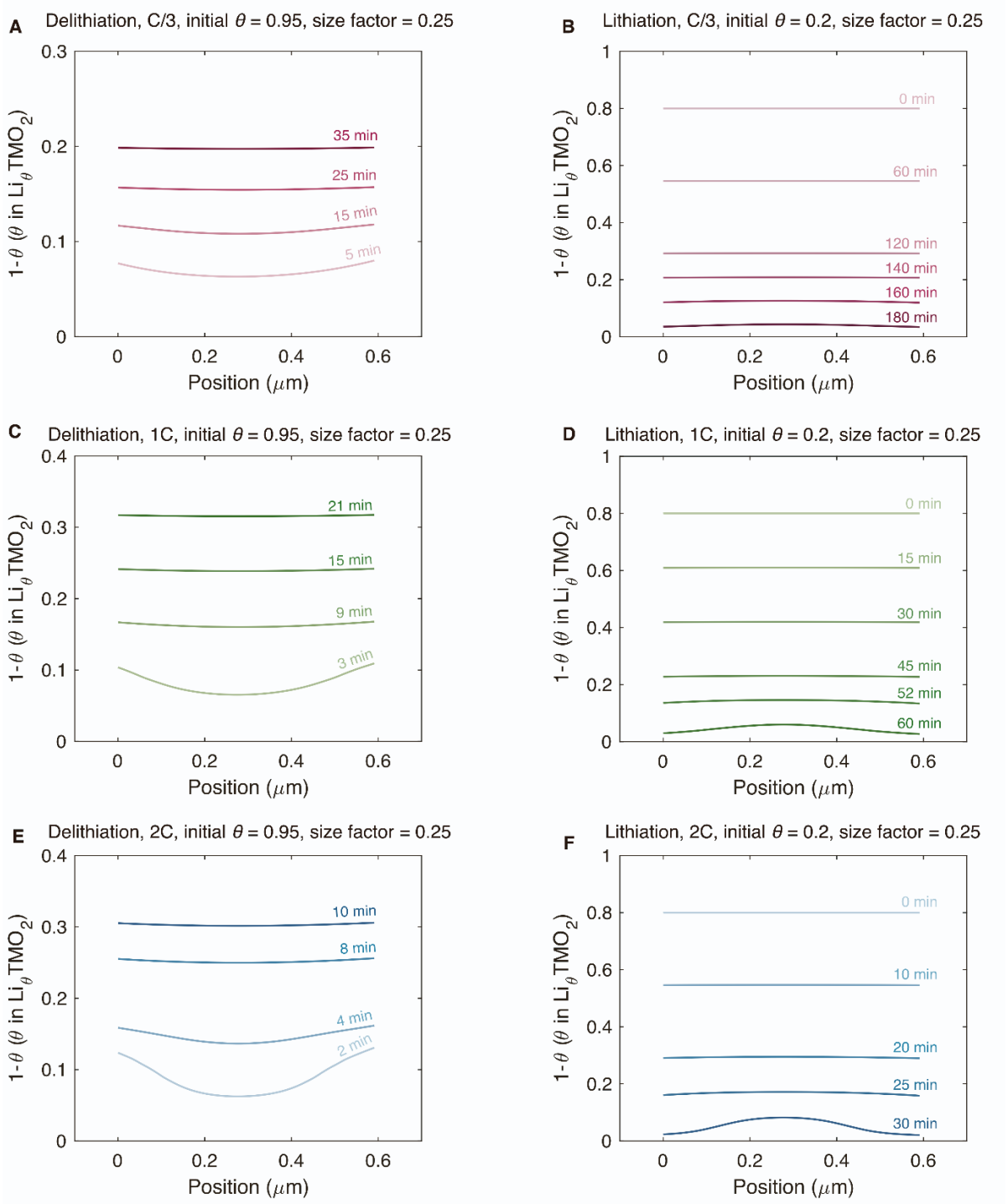

Figure S15. Effect of particle size on the lithium heterogeneity (size factor, 0.25). Modelling results showing the spatio-temporal variation of the degree of delithiation at: (**A**) C/3, (**C**) 1C, (**E**) 2C; and lithiation process: (**B**) C/3, (**D**) 1C, (**F**) 2C for a particle size of 600 nm and $D_{\mathrm{Li}}^{\mathrm{eff}} = D_{\mathrm{Li}}/3.5$. Lithium occupancies are approximately uniform across the particle for C-rates up to 2C.

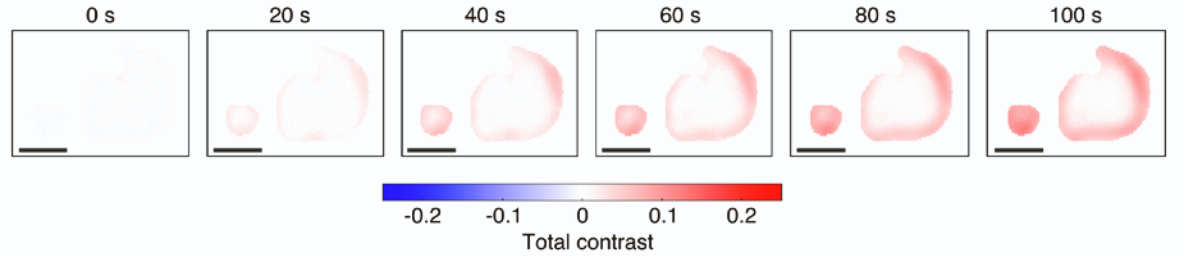

Figure S16. Particle size effect on the lithium heterogeneity. Lithium heterogeneity in particles with different sizes at the beginning of delithiation at 2C. Scale bar, 1 µm.

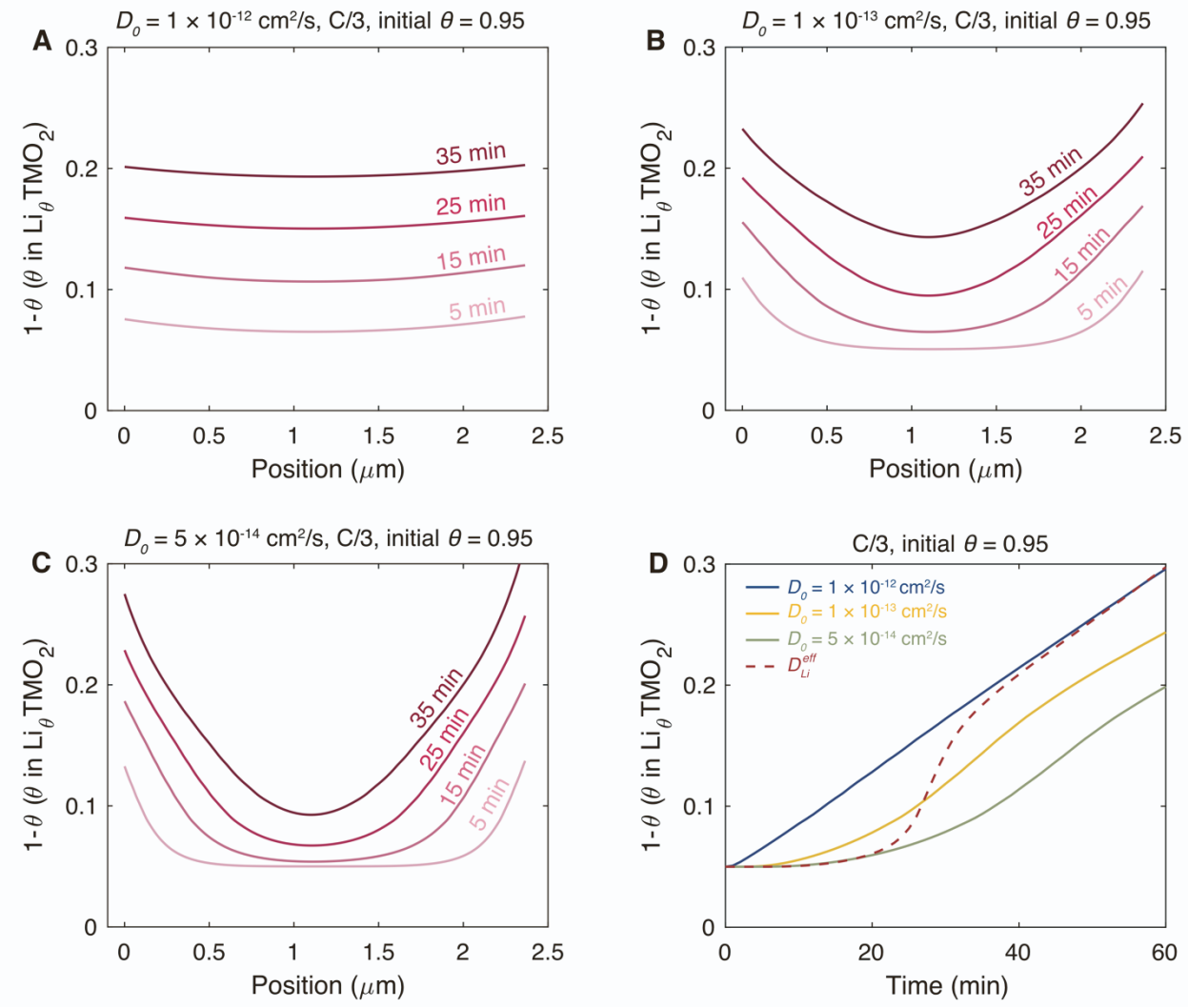

Figure S17. Constant diffusion coefficient vs SOC dependent diffusion coefficient. Modelling results showing the spatio-temporal variation of the degree of delithiation at a charge rate of C/3 along the line marked in **Figure 3C** for different choices of a constant diffusion coefficient D_0 that is independent of the SoC. (**A-C**) Degree of delithiation within the particle with (A) D_0 =

1×10^{-12} cm^2 s^{-1} , (B) $D_0 = 1 \times 10^{-13}$ cm^2 s^{-1} and (C) $D_0 = 5 \times 10^{-14}$ cm^2 s^{-1} . (**D**) Corresponding temporal variation of the degree of delithiation at the particle centre (position marked by dashed line in **Figure 3D**) using constant D_0 values (**A-C**). We include predictions using $D_{\mathrm{Li}}^{\mathrm{eff}}$ to illustrate the very different behaviour compared to the constant D_0 values. No single constant value of D_0 can capture the experimental observation of an initial delay in delithiation at the particle centre followed by fast delithiation. However, this experimental feature is well reproduced for $D_{\mathrm{Li}}^{\mathrm{eff}} = D_{\mathrm{Li}}/3.5$ (see **Figure S2C**).

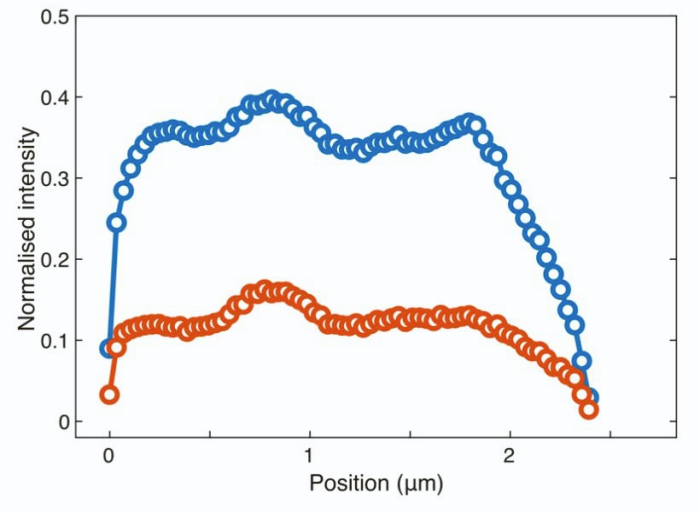

Figure S18. Line plots of the normalised intensity as a function of position at the end of CC discharge. Blue curve: 1C rate. Red curve: after an additional two-hours voltage hold at 3 V.

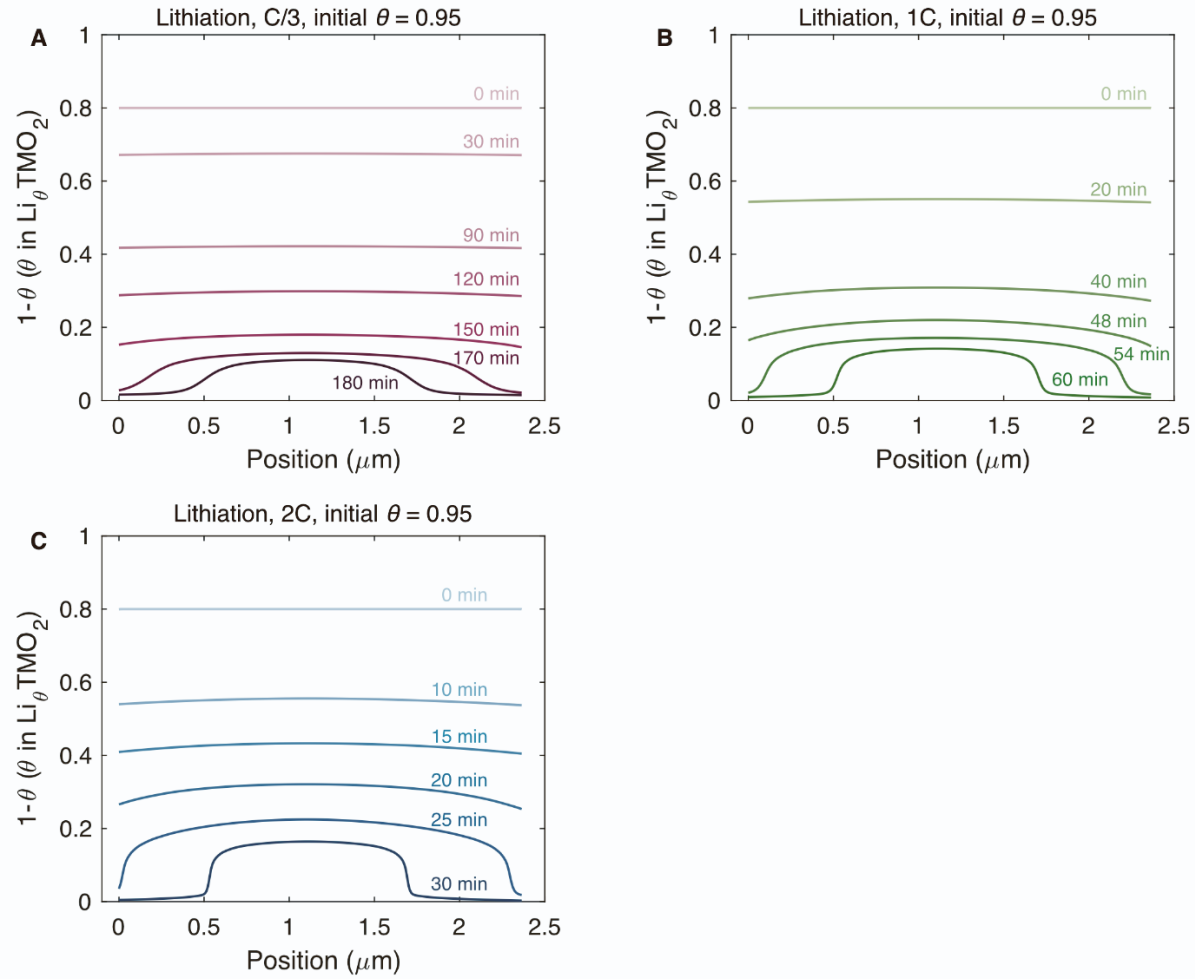

Figure S19. Modelling lithium heterogeneity at the end of lithiation. Modelling results showing the spatio-temporal variation of the degree of delithiation at (**A**) C/3, (**B**) 1C and (**C**) 2C, along the horizontal line marked in **Figure 3C** with $D_{\mathrm{Li}}^{\mathrm{eff}} = D_{\mathrm{Li}}/3.5$. Significant lithium heterogeneities are observed when the occupancy in the particle exceeds $\theta = 0.8$ $(1 - \theta = 0.2)$, caused by a drop in the diffusivity to the order of 10^{-13} $\mathrm{cm}^2\ \mathrm{s}^{-1}$. The occupancy at the particle centre lags significantly behind the surface near the end of lithiation for all three C-rates, with 2C showing the largest gradient across the particle.

It is observed that the gradient in occupancy approaches zero near the particle surface as the surface fully lithiates, i.e. $\theta \to 1$. From Figure S1A, it can be observed that V_{oc} rapidly drops as $\theta \to 1$. This results in a higher flux **J** (**J** $\propto \partial V_{\mathrm{oc}}/\partial\theta$ from Equation 12) at these spatial locations when compared to the time points before the end of lithiation where V_{oc} changes gradually with θ. The increase in **J** drives the incoming Lithium faster towards the particle core resulting in minor changes in occupancy near the particle surface as seen in the occupancy distribution, see for example the 170 min and 180 min cases in Figure S19A. These results imply that the effect of the increase in **J** due to the non-linearity in the chemical potential dominates near full lithiation over the lower $D_{\mathrm{Li}}^{\mathrm{eff}}$ in this occupancy range.

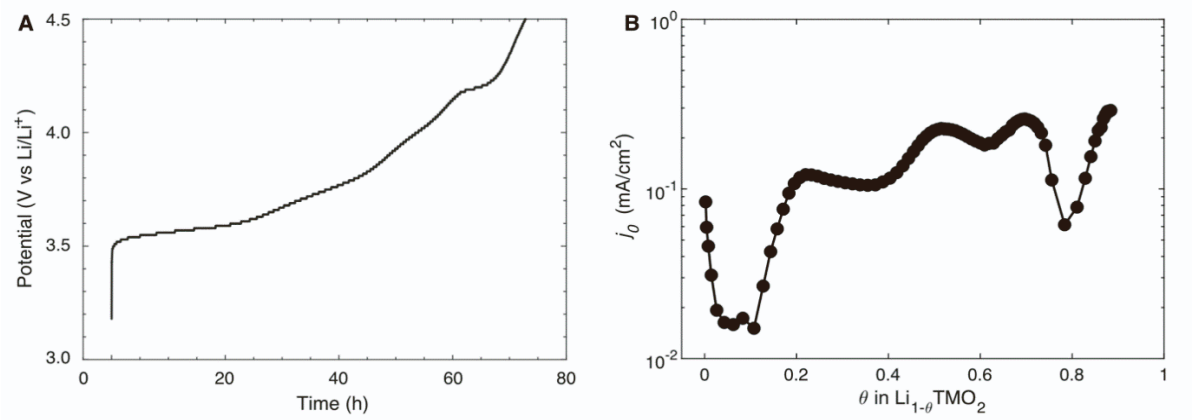

Figure S20. Potentiostatic intermittent titration technique (PITT) results. (**A**) Voltage profile obtained from PITT experiment. (**B**) Exchange current density as a function of SoC.

Potentiostatic intermittent titration technique (PITT) experiments were conducted using the Potentiodynamic Cycling with Galvanostatic Acceleration (PCGA) method on a Biologic VSP300 potentiostat with a stepwise potential scan of 10 mV and a minimum current limit of the equivalent of C/200 (that is, 1.05 mA g^{-1}). For each voltage step, the current response was plotted in the form of ln*I* versus *t* and linear fitting was performed (using the MATLAB curve fitting toolbox) to obtain the slope and vertical intercept to determine the exchange current densities.[18,19]

REFERENCES:

1. Merryweather, A. J.,Schnedermann, C.,Jacquet, Q.,Grey, C. P., and Rao, A. (2021**)**. Operando optical tracking of single-particle ion dynamics in batteries. Nature *594*, 522-528. DOI:10.1038/s41586-021-03584-2
2. Deng, Y., and Chu, D. (2017**)**. Coherence properties of different light sources and their effect on the image sharpness and speckle of holographic displays. Scientific Reports *7*, 5893. DOI:10.1038/s41598-017-06215-x
3. Märker, K.,Reeves, P. J.,Xu, C.,Griffith, K. J., and Grey, C. P. (2019**)**. Evolution of Structure and Lithium Dynamics in $LiNi_{0.8}Mn_{0.1}Co_{0.1}O_2$ (NMC811) Cathodes during Electrochemical Cycling. Chem. Mater. *31*, 2545-2554. DOI:10.1021/acs.chemmater.9b00140
4. Hung, I.,Zhou, L.,Pourpoint, F.,Grey, C. P., and Gan, Z. (2012**)**. Isotropic High Field NMR Spectra of Li-Ion Battery Materials with Anisotropy >1 MHz. J. Am. Chem. Soc. *134*, 1898-1901. DOI:10.1021/ja209600m
5. Trevisanello, E.,Ruess, R.,Conforto, G.,Richter, F. H., and Janek, J. (2021**)**. Polycrystalline and Single Crystalline NCM Cathode Materials—Quantifying Particle Cracking, Active Surface Area, and Lithium Diffusion. Adv. Energy Mater. *n/a*, 2003400. DOI:10.1002/aenm.202003400
6. Logan, E. R.,Hall, D. S.,Cormier, M. M. E.,Taskovic, T.,Bauer, M.,Hamam, I.,Hebecker, H.,Molino, L., and Dahn, J. R. (2020**)**. Ester-Based Electrolytes for Fast Charging of Energy Dense Lithium-Ion Batteries. J. Phys. Chem. C *124*, 12269-12280. DOI:10.1021/acs.jpcc.0c02370
7. Grey, C. P., and Dupré, N. (2004**)**. NMR Studies of Cathode Materials for Lithium-Ion Rechargeable Batteries. Chem. Rev. *104*, 4493-4512. DOI:10.1021/cr020734p
8. Pan, C.,Lee, Y. J.,Ammundsen, B., and Grey, C. P. (2002**)**. ^{6}Li MAS NMR Studies of the Local Structure and Electrochemical Properties of Cr-doped Lithium Manganese and Lithium Cobalt Oxide Cathode Materials for Lithium-Ion Batteries. Chem. Mater. *14*, 2289-2299. DOI:10.1021/cm011623u
9. Trease, N. M. et al. (2016**)**. Identifying the Distribution of Al^{3+} in $LiNi_{0.8}Co_{0.15}Al_{0.05}O_2$. Chem. Mater. *28*, 8170-8180. DOI:10.1021/acs.chemmater.6b02797
10. Norris, J. R. (1967**)**. Rapid computation of magnetic resonance line shapes for exchange among many sites. Chem. Phys. Lett. *1*, 333-334. DOI:10.1016/0009-2614(67)80009-5
11. Zeng, D.,Cabana, J.,Bréger, J.,Yoon, W.-S., and Grey, C. P. (2007**)**. Cation Ordering in $Li[Ni_xMn_xCo_{(1-2x)}]O_2$-Layered Cathode Materials: A Nuclear Magnetic Resonance (NMR), Pair Distribution Function, X-ray Absorption Spectroscopy, and Electrochemical Study. Chem. Mater. *19*, 6277-6289. DOI:10.1021/cm702241a
12. Harris, K. J.,Foster, J. M.,Tessaro, M. Z.,Jiang, M.,Yang, X.,Wu, Y.,Protas, B., and Goward, G. R. (2017**)**. Structure Solution of Metal-Oxide Li Battery Cathodes from Simulated Annealing and Lithium NMR Spectroscopy. Chem. Mater. *29*, 5550-5557. DOI:10.1021/acs.chemmater.7b00836
13. Lončarević, I.,Dujak, D.,Jakšić, Z. M.,Karač, A.,Budinski-Petković, L., and Vrhovac, S. B. (2019**)**. Anomalous tracer diffusion in the presence of extended obstacles on a triangular lattice. Physica A: Statistical Mechanics and its Applications *527*, 121258. DOI:10.1016/j.physa.2019.121258

14. Li, H.,Zhang, N.,Li, J., and Dahn, J. R. (2018**)**. Updating the Structure and Electrochemistry of Li_xNiO_2 for $0 \leq x \leq 1$. J. Electrochem. Soc. *165*, A2985-A2993. DOI:10.1149/2.0381813jes
15. de Biasi, L.,Schiele, A.,Roca-Ayats, M.,Garcia, G.,Brezesinski, T.,Hartmann, P., and Janek, J. (2019**)**. Phase Transformation Behavior and Stability of $LiNiO_2$ Cathode Material for Li-Ion Batteries Obtained from In Situ Gas Analysis and Operando X-Ray Diffraction. ChemSusChem *12*, 2240-2250. DOI:10.1002/cssc.201900032
16. Grenier, A.,Liu, H.,Wiaderek, K. M.,Lebens-Higgins, Z. W.,Borkiewicz, O. J.,Piper, L. F. J.,Chupas, P. J., and Chapman, K. W. (2017**)**. Reaction Heterogeneity in $LiNi_{0.8}Co_{0.15}Al_{0.05}O_2$ Induced by Surface Layer. Chem. Mater. *29*, 7345-7352. DOI:10.1021/acs.chemmater.7b02236
17. Xu, C.,Reeves, P. J.,Jacquet, Q., and Grey, C. P. (2021**)**. Phase Behavior during Electrochemical Cycling of Ni-Rich Cathode Materials for Li-Ion Batteries. Adv. Energy Mater. *11*, 2003404. DOI:10.1002/aenm.202003404
18. Li, J.,Xiao, X.,Yang, F.,Verbrugge, M. W., and Cheng, Y.-T. (2012**)**. Potentiostatic Intermittent Titration Technique for Electrodes Governed by Diffusion and Interfacial Reaction. J. Phys. Chem. C *116*, 1472-1478. DOI:10.1021/jp207919q
19. Tsai, P.-C.,Wen, B.,Wolfman, M.,Choe, M.-J.,Pan, M. S.,Su, L.,Thornton, K.,Cabana, J., and Chiang, Y.-M. (2018**)**. Single-particle measurements of electrochemical kinetics in NMC and NCA cathodes for Li-ion batteries. Energy Environ. Sci. *11*, 860-871. DOI:10.1039/c8ee00001h